Tidal contributions to shelf break dynamics in the South-western Tropical Atlantic

Syumara Queiroz[1,2], Marcus André Silva[1,2], Moacyr Araujo[1,2,3], Alex Costa da Silva[1,2] & Arnaud Bertrand[1,2,4]

[1]Laboratório de Oceanografia Física Estuarina e Costeira (LOFEC), Department of Oceanography, Universidade Federal de Pernambuco, Av. Arquitetura, 50740-550, Recife, Pernambuco, Brazil.

[2]IJL TAPIOCA: International Joint Laboratory - Tropical Atlantic Interdisciplinary laboratory on physical, biogeochemical, ecological and human dynamics. Federal University of Pernambuco, Av. Arquitetura, 50740-550, Recife, Pernambuco, Brazil.

[3]Brazilian Research Network on Global Climate Change – Rede CLIMA, 12227-010, São José dos Campos, São Paulo, Brazil.

[4]Institut de Recherche pour le Développement (IRD), MARBEC (Univ Montpellier, CNRS, Ifremer, IRD), 34203 Sète, France.

Corresponding author: Syumara Queiroz (syumaraqueiroz@hotmail.com)

Preprint not peer reviewed

This preprint research paper has not been peer reviewed. Electronic copy available at: https://ssrn.com/abstract=4861987

Abstract

Tidal currents and western boundary currents play an important role in the shelf-break/slope (SBS) transition, where processes occurring at a variety of temporal and spatial scales can interact enhancing biological productivity. In the southwestern tropical Atlantic (SWTA), the North Brazil Undercurrent (NBUC), was previously reported to induce uplift along the slope. In this work we investigated the high frequency temporal and spatial-scales of the shallow (15-59 m) along- and cross-shelf velocities in a SBS transition in the SWTA. The data was obtained from the Multiple Rectangles Transect (MRT) experiment, where continuous (every 2 min) measurements of currents were made crossing the shelf-break repeatedly during a timeframe of 26 hours. The variability was analyzed through adaptative signal analysis methods, and we investigated if the observed patterns contributed to uplift variability on a short timeframe from hydrographic profiles. Results showed that tidal forcing was the main responsible for the variability of the along- and cross-shelf currents in different scales. Cross-shelf patterns of divergence/convergence during flood/ebb, expected from the tidal forcing, were amplified or reduced by the effect of stronger or weaker along-shelf current on the slope; and flood timing for cross-shelf flow was coherent with uplifted waters reaching the shelf-edge stations. Local variability of uplift intensity was related to tidal forcing added to the currents of the NBUC's upper limit. While there was no stronger uplift during the high tide (in relation to climatologic patterns), the decrease of the along-shelf velocity during low tide, resulted in decrease of uplift. Therefore, tidal forcing appears as an important process to be considered in uplift mechanisms for the western boundary system in question. Still, more investigation is needed, since our dataset was limited and there are open questions about SBS dynamics enhancing productivity in the SWTA.

Keywords: Uplift. Cross-shelf flows. Tides. Adaptive Signal Analysis. Western Boundary System. Brazil, Northeast, Pernambuco.

1 Introduction

In the continental margin, the shelf-break is the "the line along which there is a marked increase in slope at the seaward margin of a shelf" (IHO, 2019), and the continental slope is "the sloping region that deepens from a shelf to the point where there is a general decrease in gradient" (IHO, 2019). An example of the shelf break and slope features is shown in **Figure 1**. Together, the shelf-break/slope (hereafter, SBS) mark the transition between the shallow and the deep ocean, where processes occurring at a variety of temporal (hours to months) and spatial scales (meters to tens of kilometers) interact, enhancing biological productivity (Huthnance, 1995; Acha et al., 2004; Genin, 2004). One of the main oceanic flows interacting with SBS features are the Western Boundary Currents (WBCs). They play an important role in climate (Wu et al., 2012; Hu et al., 2015; Shears and Bowen, 2017), ocean mixing (Jing and Wu, 2014; Nagai et al., 2017) and complex nonlinear dynamic terms in low latitudes regions (Holland, 1972; Huthnance, 1984; Nagai et al., 2017). Interaction between WBCs and topography can alter water-mass characteristics towards the shelf and/or to the ocean through the generation of eddies, meanders, fronts and horizontal shear (Gawarkiewicz, 1991; Huthnance, 1995; Gula at al., 2015), or by driving orographic upwelling (Oke and Middleton, 2000; Roughan and Middleton 2002; Castelao, 2011).

Tidal currents also play an important role in SBS dynamics by interacting with the topography, generating internal tides that can propagate along the platform or be reflected at the SBS towards the ocean (Cacchione, 2002; Lamb, 2013). The processes of tidal energy dissipation when it reaches the continental slope are still under investigation (Nash et al., 2007; Martini et al., 2011; Legg, 2014) but

Preprint not peer reviewed

This preprint research paper has not been peer reviewed. Electronic copy available at: https://ssrn.com/abstract=4861987

internal-wave collapse on the shelf-break is known to dissipate energy and can cause the rising of the thermocline or even break the stratification (Navrotsky et al., 2004; Grados et al., 2016; Nazarian and Legg, 2017). Additionally, interactions between tides and internal waves can affect the background current dynamics (e.g., WBCs; Davis et al., 2008; Nagai et al., 2017; Prestes et al., 2018) increasing the complexity of SBS processes.

Western boundary current dynamics over the SBS can induce cross-shelf flows through Ekman bottom transport, current separation from the shelf break (turning offshore), bottom-hugging shelf edge eddies and shelf-break fronts (Brink, 2016). Even when the velocity of the cross-shelf flow is of one order of magnitude smaller than the along-shelf flow (e.g., in WBCs regime), it can represent substantial transport across isobaths, influencing water stratification, exchanges between open sea and shelf waters, and the mixing and/or water-masses entrainment (Schaeffer et al., 2013; Brink, 2016). The cross-shelf flow can carry saltier and colder waters towards the shelf, uplifting nutrients into the euphotic zone, enhancing primary production (Fournier et al., 1977; Marra et al., 1990; Mizobata et al., 2008), and favoring mass and energy transfer to the upper trophic levels (Schneider, 1982; Munk et al, 1995). This potential cross-shelf transport can also contribute to ocean-atmosphere mass and heat fluxes, which are important for weather and climate variability (Huthnance, 1995; Silva et al., 2009a; Gawarkiewicz et al., 2018).

The complexity of the multiscale processes interacting on the SBS hampers the collection of data comprehensively representing the hydrodynamics and traditional sampling design are usually not be adapted enough to capture these dynamics (Brink, 2016). While ocean models and remote sensing methods have been key in understanding larger scale processes (Joseph, 2014; Fox-Kemper et al., 2019) there is still a need for observations at small scales (e.g., Bertrand et al., 2014; Grados et al., 2016; Lévy et al., 2018) to improve the knowledge of meso- and submesoscale dynamics (Fox-Kemper et al., 2019).

Two important processes that can happen on the SBS are the uplift and upwelling, related to slope currents dynamics along the slope feature (Matano e Palma, 2008; Aguiar et al., 2014; 2018). The term uplift refers to the raising of cold water towards a certain depth, however, not reaching the surface, while upwelling happens when the uplifted water outcrops, reaching the surface (Rochford, 1991). More recently, a work by Silva et al. (2021) revealed uplift (instead of upwelling) along the continental slope in Northeast Brazil, that they related to the North Brazil Undercurrent (NBUC) flow interaction with the slope topography. The NBUC is a low latitude WBC that arises from the bifurcation of the southern branch of the South Equatorial Current (sSEC) when it reaches the Brazilian coast (**Figure 1a**) (Schott et al., 2002, 2005; Silva et al., 2009a; 2009b). Together with the North Brazil Current (NBC), the NBUC plays an important role in the inter-hemispheric heat transport as a part of the upper south equatorial limb of the Atlantic Meridional Overturning Circulation (AMOC) (Schott et al., 2002; Veleda et al., 2011). Still, there is a lack of information about the high frequency variability of the NBUC and how tidal forcing acts on the shelf break region in the Northeastern Brazilian waters and how the tides might influence the uplift on the SBS.

Considering the importance of the SBS in this region, the objective of the present work is to describe high frequency temporal and spatial patterns of the shallow along-shelf and cross-shelf currents in a shelf-break/slope transition. We investigated the dominant high frequency (period larger than 2 min and lower than 26h) flow variability on the upper water column (15-59 m) and if/how the observed patterns contribute to uplift variability on observed from *in situ* measurements in short timeframe. For this we used data obtained from a sampling strategy first presented in Bertrand et al. (2008a), here, onwards denominated Multiple Rectangles Transect (MRT). The experiment was executed in Pernambuco continental margin, in Northeast Brazil. In this region, the shelf-break is found between

This preprint research paper has not been peer reviewed. Electronic copy available at: https://ssrn.com/abstract=4861987

around 60 m deep (Camargo et al., 2007), the slope extends from this depth until the Pernambuco Plateau upper level (~700 m) (Zembruscki et al., 1972; Coutinho, 1996) and NBUC is the main along shelf current ruling the dynamics over the slope (Hummels et al., 2015; Araujo et al., 2019; Dossa et al., 2021). In addition, regional oceanic reanalysis product provided a framework for the hydrodynamics settings in the study region, since or dataset is time and space restricted.

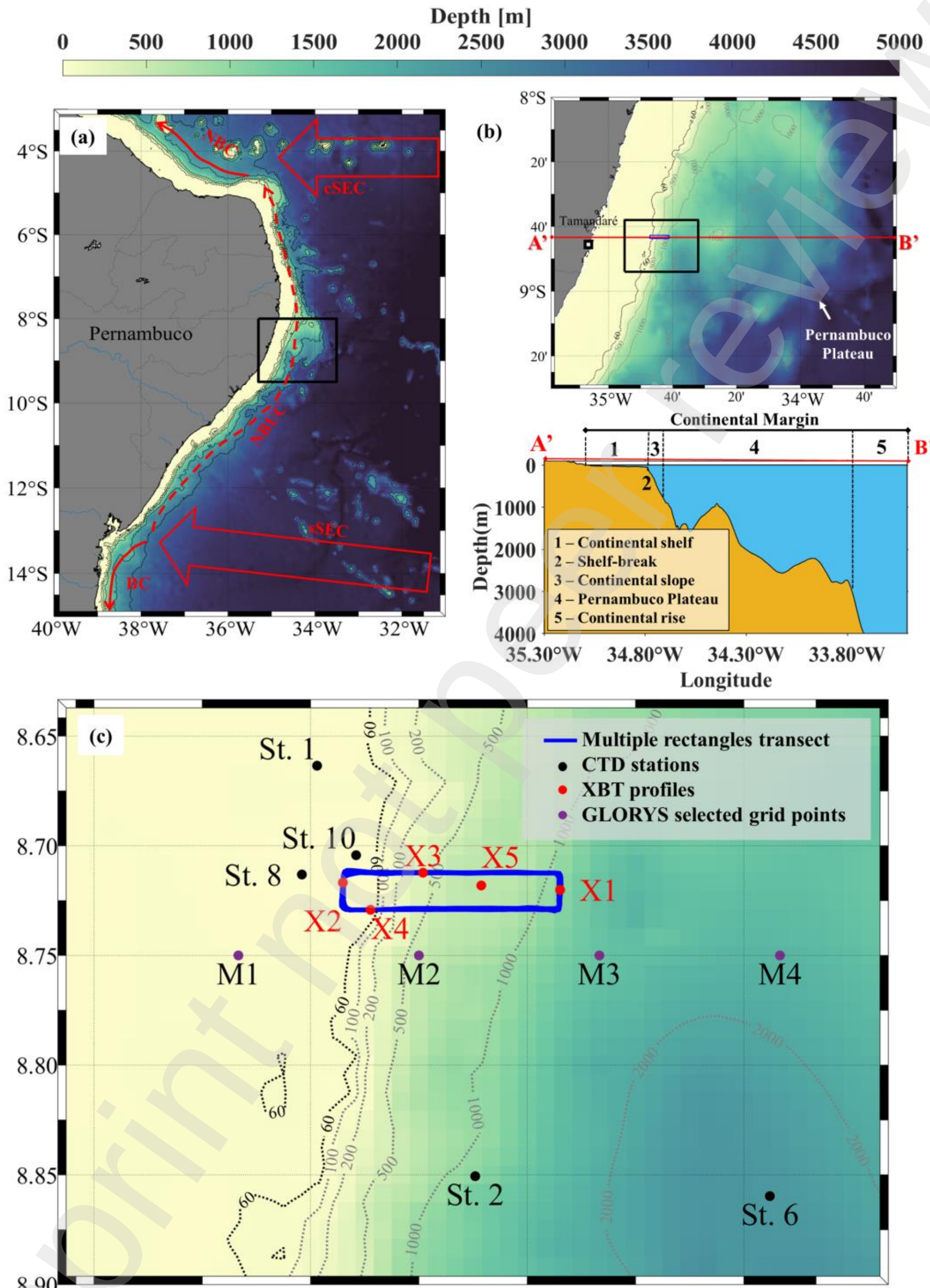

Figure 1. (a) Schematic representation of the general circulation of Northeast Brazil. The Zonal currents are represented by the central and southern branch of the South Equatorial Current (cSEC and sSEC) (wide red arrow); sSEC mean bifurcation position is around 13°S; Western boundary currents are represented by the superficial North Brazil Current (NBC) and Brazil Current (BC) (narrow red arrow) and sub superficial North Brazil Undercurrent (NBUC) (narrow red dashed arrow). Black box highlights the Pernambuco continental margin (PCM) and the Pernambuco Plateau (PP) showed in **(b).** Bottom panel in **(b)** shows the bottom configuration of the PCM along a cross-section (A'-B') at the same latitude of the Multiple rectangles transect (MRT). The flat bottom from the shelf (1) is interrupted at the shelf-break depth (2), around 60m, by the steep isobaths of the slope

Preprint not peer reviewed

This preprint research paper has not been peer reviewed. Electronic copy available at: https://ssrn.com/abstract=4861987

(3). The slope is in turn interrupted by the PP (4), located between the 700 and 3000m isobaths and, bellow this depth the continental rise (5) precedes the deep ocean. The highlight **(**black box) in the map in **(b)** is the study region in **(c)** were the MRT experiment (blue solid line) take place. The black, red and purple dots indicate the position of the CTDO stations, XBT profiles, and selected GLORYS grid points, respectively. Bottom depth for this Figure was extracted from the 30" arc GEBCO data (Weatherall et al., 2015).

2 Materials and Methods

2.1 In situ data and processing

In this work, we used data from the multiple rectangles transect (MRT) experiment to study the along-scale hydrodynamic variability in play in the shelf-break/slope (SBS) transition of a WBC in the Southwestern Tropical Atlantic. The study area (**Figure 1a**) is inserted in the southwest tropical Atlantic, where the NBUC is one of the main WBC interacting with the SBS features (Stramma et al., 1995; Schott et al., 2002, 2005; Dossa et al., 2021). The multiple rectangles transect (MRT) experiment took place in a shelf-break/slope transition, where the slope inclination is interrupted by the Pernambuco Plateau (**Figure 1b**) (Buarque et al., 2016). The dataset was collected in April 2017 over the northeast Brazilian continental shelf-break and adjacent slope during the ABRAÇOS 2 survey (Bertrand, 2017).

The MRT experiment consisted in 2 by 11 km side rectangular transects (**Figure 1c**) performed repeatedly for about 26 hours (from April 11th 19:17 to April 12th 20:45, UTC). Each repetition took about 1h45 resulting in 15 rectangles. With this approach, we obtained a time-space varying information within a daily cycle and around two semidiurnal spring-tide cycles. To demonstrate how the multiple rectangles transect data acquisition works, we present a time lapse of the location and track of the ship during the transect execution while the information of bottom depth and current velocity (along- and cross-shelf) is acquired in Supp. Video 1.

Data continuously recorded during the MRT transects consisted of, sea surface temperature (SST) and salinity (SSS), wind speed and direction, current velocity (zonal and meridional components), and high-resolution bathymetry. Only the last two were raw and required processing for the purposes of this work. We manually corrected the bathymetry was manually corrected using the Matecho software (Perrot et al., 2018). The 2 min ensemble raw current velocity data was processed using the CASCADE tools following Herbert et al. (2015). However, the current was not de-tided since we intended to analyze its intrinsic natural variability and the adaptative method capacity to separate the tidal signal from the original data. Instead, we used the predicted tidal current from the TPXO9-atlas (Egbert and Erofeeva, 2002; Erofeeva, 2022) tidal model only to compare with observational current data after the decomposition. The barotropic tidal currents and tidal amplitude were estimated from the semidiurnal dominant components (M_2, S_2, K_2 and N_2) for each point in space and time of the MRT data.

After the data processing, we corrected the zonal and meridional components, for each depth level, in relation to the adjacent slope orientation from the high-resolution bathymetric data. This was done to obtain the real along-shelf and cross-shelf components from the observed currents. First, the tangent between the two zonal transects of the MRT was calculated to obtain the angle (θ) in relation to the meridional direction. Then the correction for the meridional and zonal currents was applied following the system of equations bellow (Brink, 2016), where U and V are, respectively the zonal and meridional component, and CS and AS are the resulting local cross-shelf and along-shelf components. The same correction procedure was applied to obtain the cross-shelf (CS-TIDE) and along-shelf (AS-TIDE) components from the tidal model prediction for comparison with the observational data.

This preprint research paper has not been peer reviewed. Electronic copy available at: https://ssrn.com/abstract=4861987

$$\begin{cases} CS = U\ \cos\theta + V\ \sin\theta \\ AS = -\ U\ \sin\theta + V\cos\theta \end{cases}$$

In this work we will present only the CS and AS components averaged for the first 15-59 m and every 2 minutes observation, thereafter the CS_{avg} and AS_{avg}, respectively. Limiting this depth above the shelf-break depth (~60m) we obtain a continuous time-series to be decomposed by the adaptative method presented in the next section.

In addition to the MRT continuous data, five quality-controlled Conductivity Temperature Depth (CTD) profiles (St. 1, 2, 6, 8 and 10; **Figure 1c**) were chosen to characterize water masses and the thermohaline structure near the MRT experiment location. Additional temperature profiles were acquired from expendable bathythermographs (XBT) during (X1 to X4; see **Figure 1c**) or just after (X5) the MRT experiment. Furthermore, as the dataset of the MRT experiment, is restricted to a small time-space scale, we complemented our dataset with monthly averaged reanalysis product in a larger spatial domain to characterize the local hydrodynamics in a regional context. Since the conditions observed in austral fall 2017 during ABRAÇOS 2 survey are representative of canonical fall conditions (Assunção et al., 2020; Dossa et al., 2021), we considered the regional context from climatological conditions. April's climatology for hydrodynamics was used as the reference for the MRT experiment. Climatology for temperature, salinity, and currents were obtained from the monthly averaged reanalysis product GLORYS (Copernicus Marine Service) from 1993 to 2019. In addition, to compare CTD and XBT vertical termohaline structure and water masses, we selected four grid points (M1 to M4 in **Figure 1c**) close to the MRT. For more information about the data used in this work see Data availability section.

2.2 MRT Timeseries analysis

The Ensemble Empirical Mode decomposition (EEMD) (Wu and Huang, 2009) was applied to separate the main timescales of the current velocity components (AS_{avg} and CS_{avg}) and tidal model current velocity components (AS-TIDE and CS-TIDE). The timescales resulting from the decomposition were obtained through the python EEMD module of the PyEMD package (https://github.com/laszukdawid/PyEMD). The main IMFs from AS_{avg} and CS_{avg} were compared with the IMFs from tidal forcing (AS-TIDE and CS-TIDE) because the tidal forcing was was relevant for the observational data variability. Additionally, since the data is changing in time and space it is expected to have spatial scales associated with the timescales observed. Therefore, the main IMFs were also used to characterize AS_{avg} and CS_{avg} variability in relation to the spatial configuration (on the shelf, shelf-break, or slope). This was achieved through the correlation obtained from Time-dependent Intrinsic Correlation (TDIC) (Chen et al., 2010; Huang and Schmitt, 2014) method with the main variability mode of bottom depth (BOT) resulting from EEMD decomposition. Applying the EEMD to the bottom depth acquired at the same time as the MRT currents allows the extraction of the larger inclination feature (shelf/shelf-break/slope) and remove the “noise” from small scale features. Additionally, the decomposition is mandatory to perform the cross-correlation of bottom depth with the current IMFs, since the TDIC works under the assumption that both signals to be correlated are IMFs. Lastly, we applied the Hilbert Transform to obtain the Hilbert Spectrum for AS_{avg} and CS_{avg}. The EEMD and the TDIC methods are reviewed in the Appendix 1. The MATLAB TDIC code we used in this work is freely available from the repository in https://doi.org/10.5281/zenodo.9748.

Preprint not peer reviewed

This preprint research paper has not been peer reviewed. Electronic copy available at: https://ssrn.com/abstract=4861987

3 Results and discussion

The results and discussion are presented considering (3.1) the hydrodynamic features depicted from the CTD, XBT stations and compared with the expected climatological patterns, (3.2) the circulation patterns during the MRT experiment and current variability observed from the timeseries analyses and (3.3) the summary of the observed tidal contribution observed in our results.

3.1 Hydrodynamic setting

The MRT was performed in April (fall) 2017 during a full-moon high tide regime (local maximum amplitude of 1 m). For the CTD stations, Temperature-Salinity (**Figure 2a**), and Salinity-O_2 (**Figure 2b**) diagrams, were used to assist water mass identification. In our study region at the Southwestern Tropical Atlantic, the NBUC extends from the near surface down to about 1100 m (Schott et al. 2005). However, as we are interested in the shallow dynamics, we restrict our observations to 100 m. The characteristic water masses down until this depth are the Tropical Atlantic Water (TW) follow by the Subtropical Underwater (STUW) and the South Atlantic Central Water (SACW). The TW is characterized by temperature higher than 25°C and σ=23-24.5 $kg.m^{-3}$ (Urbano et al., 2008). The STUW also called the Salinity Maximum Water is characterized by maximum salinity values (>36.5), σ_θ slightly below 25 $kg.m^{-3}$ and by the and high oxygen content (Stramma and England, 1999; Urbano et al., 2008). The SACW presents temperatures between 10-23°C, salinity >35 and potential density between 24.5-27 $kg.m^{-3}$ (Stramma and England, 1999).

The water masses from the CTD stations presented characteristic consistent with the mixture of the warm TW with the oxygen- and salinity-rich STUW in the first 100m (**Figure 2a,b**) agreeing with the climatology. **Figure 2c** shows that close to the MRT (Lat: 8.75°S and Lon: 35.8-34.5°W) from the surface to 100 m the salinity was higher than 36.5. This means that the STUW outcrops in this region, transported by the NBUC that shallows as it flows to low latitudes, as shown by the salinity and current velocity in **Figure 2d,e**. Below this water mass down to 500 m, we identified the South Atlantic Central Water (SACW) (not shown).

Preprint not peer reviewed

This preprint research paper has not been peer reviewed. Electronic copy available at: https://ssrn.com/abstract=4861987

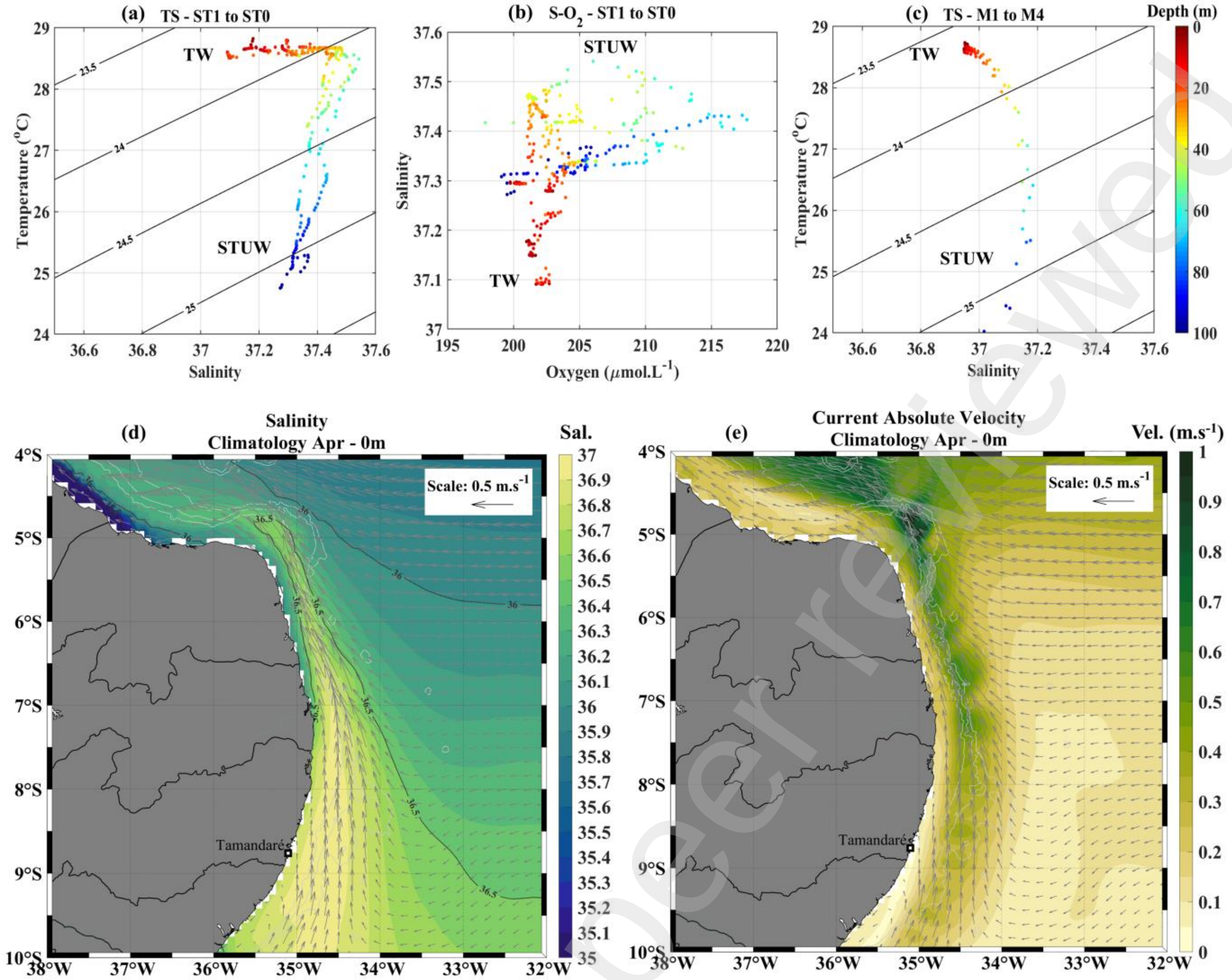

Figure 2. (a) T-S and **(b)** S-O_2 diagrams for CTD stations (0-100m); **(c)** T-S diagram for selected grid points of the climatology (M1 to M4 in **Figure 1c**). Diagrams show the presence of the mixing between Atlantic Tropical water (TW) and Subtropical underwater (STUW). Climatology of surface **(d)** salinity **(e)** current velocity**;** grey arrows represent current direction.

The thermohaline structure from CTD (**Figure 3a-d**) profiles for the first 100m (see Supp. Figure S1 for complete profiles) shows that, due to the weak vertical salinity gradient (**Figure 3c**), temperature controlled the density stratification of the upper layers (**Figure 3d**). In this manner, the isothermal layer was equivalent to the mixed layer (ML) and the temperature profiles depicted three distinct thermal patterns (**Figure 3e**):

(i) Well mixed (shallow St. 1)

(ii) Isotherm uplift (shelf stations St. 8 and St. 10 – performed just before and after the MRT, respectively)

(iii) Profiles with stepwise vertical structure (shelf station St. 10; deeper stations St. 2 and 6).

The stations closer to the shelf break (St. 2 and St. 10) presented more pronounced thermocline staircase profiles and shallower ML. As in the work by Silva et al. (2021), we also observed uplift of colder waters on the slope and close to the shelf-break. In addition, the observed uplift influenced the primary productivity, as indicated by the chlorophyll-a profiles (**Figure 3d**). The peak of chlorophyll-a was close to 100 m in deeper stations (St. 2 and St.6), with slighter higher values (~0.9 $mg.m^{-3}$) for St. 2, the station closer to the shelf-break (**Figure 3g**). In shallow stations, we did not observe the peak of

Preprint not peer reviewed

This preprint research paper has not been peer reviewed. Electronic copy available at: https://ssrn.com/abstract=4861987

chlorophyll-a, that remained below 0.25 $mg.m^{-3}$, except in St. 8, one of the stations with isotherm uplift where it reached 0.45 $mg.m^{-3}$.

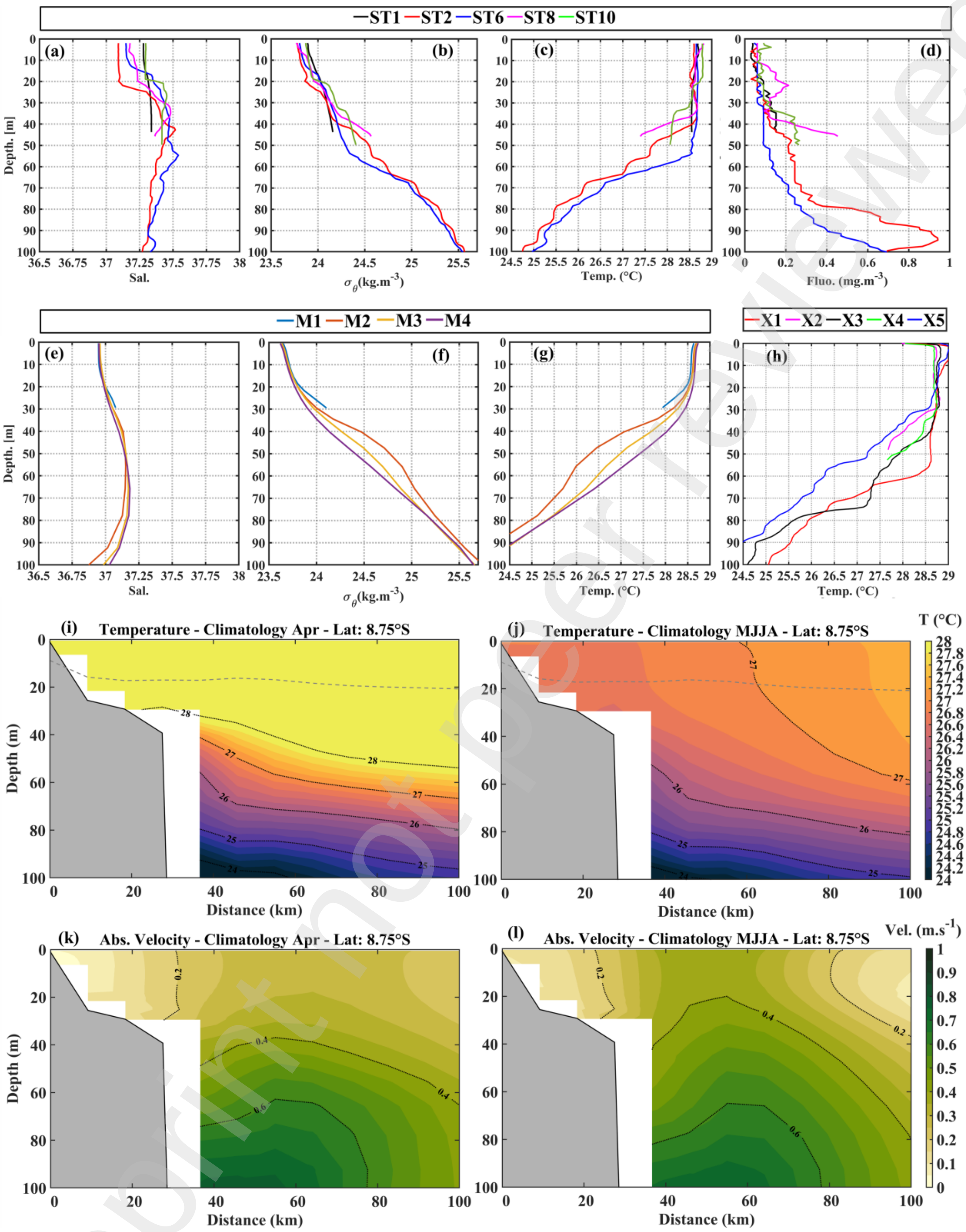

Figure 3. Vertical profiles of the first 100 m of **(a-d)** CTD stations, **(e-g)** selected GLORYS grid points and **(a)** XBT, for **(a,e)** salinity, **(b,f)** potential density anomaly, **(c,g,f)**, temperature and **(d)** chlorophyll-a concentration.

April climatology for this region shows the uplift of the isotherms adjacent to the shelf-break (**Figure 3i**), with no indication of this denser and colder water reaching the surface i.e., no upwelling. However, averaged temperature for the period of May to August (MJJA; **Figure 3j**) shows that the uplift observed in the climatology is not restricted to April. Indeed, for this period, the evidence is the uplift becomes upwelling, reaching the surface. As this uplift was previous related to the NBUC, we show

Preprint not peer reviewed

This preprint research paper has not been peer reviewed. Electronic copy available at: https://ssrn.com/abstract=4861987

current velocity down to 100m for the same period (**Figure 3k**). The current presented values ≤0.4 $m.s^{-1}$ close to the slope in the surface, and >0.4 $m.s^{-1}$ at the shelf break depth (~60m) increasing with depth reaching values >0.8 $m.s^{-1}$ at its core (150-275 m, not shown). For the period of MJJA the upwelling might be related to the swallowing of the NBUC's upper limit (**Figure 3l**).

In **Figure 3e-g**, we also presented the thermohaline structure for selected grid points of the climatology (for the locations, see **Figure 1c**). M1 is the only point on the shelf close to the shelf-break and the distance from the shelf increases oceanward from M2 to M4. The salinity from our CTD stations (**Figure 3a**) was higher than the climatology (**Figure 3e**). And, although we should expect higher density due to the higher salinity observed in the CTD stations, the potential density anomaly observed (**Figure 3b)**, agreed with the climatology (**Figure 3f**). This was due to the fact that, except for St. 2, the temperature from CTD stations (**Figure 3c**) bellow 30 m was 0.5°C higher than the expected from the climatology (**Figure 3g**).

Additional temperature profiles from XBT data are presented in **Figure 3h.** Particularly, one of the profiles (X5), launched just after the MRT survey under high tide influence, presented a minus 2°C difference in temperature when compared with the first profile (X1), performed during low tide for 60 m, in less than 5 km distance. Temperature values for X5 were also below all values found in the other CTD profiles (**Figure 3c**) for the same depths from 30 to 100 m and agreed with the climatological values (**Figure 3g**). The vertical temperature gradient was weak and the 27ºC isotherm was elevated, reaching almost 50 m deep.

The variability of temperature profiles in a small space- and timescale, mostly close to the slope, was higher than expected, leading us to conclude that some shelf-break/slope process was in play. Additionally, presence of uplifted water in St. 2 and St. 8, located close to the shelf-break, indicates that a negative cross-shelf velocity (coast-ward) exists. In a previous work by Domingues et al. (2017) a persistent cross-shelf flow towards the coast was previously reported at the region under the influence of the Pernambuco Plateau orography (**Figure 1b**). However, to our knowledge, no mechanism was proposed for this flow until now. In the next section we investigate the dynamic variability observed during the MRT experiment to find some clues about the processes in play at the SBS transition. We should add that, since we lack long term observations for this region, our inferences of why the temperature was 0.5°C higher than the climatology are limited. So, we look only to the variability between stations within our survey. However, we cannot discard that the interannual variability and/or changes due to climatic changes might be responsible for this change.

3.2 Patterns and variability during MRT experiment

The MRT observational dataset used in the present work, comprises the scale of 36 hours and few (<11km) kilometers. The wind speed was weak for the whole MRT experiment (avg. 2.05 ±0.80 $m.s^{-1}$, **Figure 4a**) with prevailing SE-S direction (62% - 29%). Additionally, during the MRT experiment, mean SSS was 37.41±0.07 with an amplitude of 0.25 (**Figure 4b**) while mean SST was 28.90±0.18°C with an amplitude of 0.73°C (**Figure 4c**), with no evidence of upwelling. This means, that a subsurface forcing for the uplift is more likely to be in play.

Preprint not peer reviewed

This preprint research paper has not been peer reviewed. Electronic copy available at: https://ssrn.com/abstract=4861987

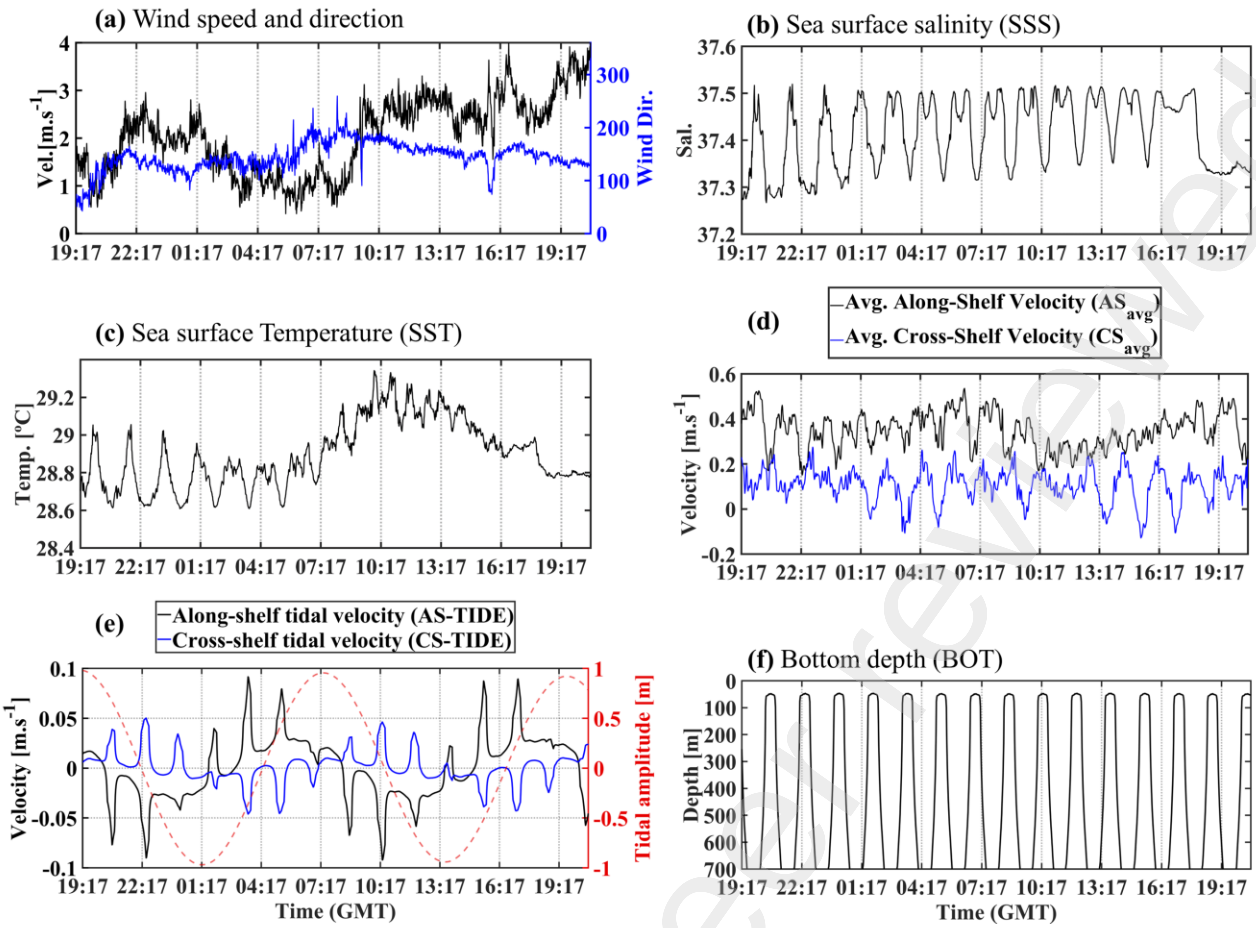

Figure 4. Multiple rectangles transect time series of **(a)** wind velocity (black solid line) and direction (blue solid line); **(b)** sea surface salinity; **(c)** sea surface temperature, **(d)** averaged (15-59 m) along-shelf velocity (AS_{avg}, black solid line) and cross-shelf velocity (CS_{avg}, blue solid line); **(e)** cross-shelf tidal velocity (CS-TIDE, blue solid line), along-shelf tidal velocity (CS-TIDE, black solid line) and tidal amplitude (red dashed line) from the tide model TPXO9 and; **(f)** bottom-depth.

The MRT experiment revealed a time-space dependent cross-shelf velocity in subsurface (**Figure 4d**) that can explain how the uplifted waters are being transported to the shelf. During the experiment, the cross-shelf average velocity (CS_{avg}, **Figure 4d**) fluctuated between ocean-ward, coast-ward, or null current (average: 0.11±0.07 m.s^{-1}, min/max -0.13/0.28 m.s^{-1}). The along-shelf velocity in the first 60 m, presented high frequency oscillations but was always positive (AS_{avg} average: 0.35±0.08 m.s^{-1}, min/max: 0.15/0.54 m.s^{-1}) (**Figure 4d**). CS_{avg} and AS_{avg} velocities have important variability related to both the tidal forcing and spatial patterns (in relation to shelf-break/slope position), that will be discussed along this section.

CS-TIDE, AS-TIDE and tidal amplitude time series predicted from de tidal model TPXO9 for the same time and location of the MRT experiment are presented in **Figure 4e**. AS-TIDE and CS-TIDE presented higher absolute velocities (±0.092 m.s^{-1} and ±0.05 m.s^{-1}, respectively) associated with flood/ebb periods with opposite patterns (**Figure 4e**). Peak positive values of AS-TIDE (negative CS-TIDE) on the shelf and weak negative AS-TIDE (positive CS-TIDE) on the slope were observed during the flood while the opposite patterns were observed during the ebb. The main direction for the tidal forcing axis was the along-shelf direction, indicated by the stronger tidal current for the AS-TIDE component (**Figure 4d**). High frequency variability observed as sharp peaks in both components are the result of the change in the location (shelf/slope) as this time series was obtained from the same track (i.e., same time and coordinates) as the MRT. This variability will be discussed further ahead.

Preprint not peer reviewed

This preprint research paper has not been peer reviewed. Electronic copy available at: https://ssrn.com/abstract=4861987

EEMD results depicted eight variability components for bottom depth (BOT) and CS_{avg} (C1 to C8) and seven variability components for AS_{avg}, CS-TIDE and AS-TIDE (C1 to C7). The original timeseries for CS-TIDE, AS-TIDE, CS_{avg} and AS_{avg} and their main variability modes, in terms of variance, are presented in **Figure 5a-d**. Their respective variance (%), averaged local period and maximum amplitude are presented in **Table 1.** Variability modes with variance below 5% did not significantly contribute to the total variability of the time-series and are therefore omitted on **Table 1** and **Figure 5** (see Supp. Table S1 and Figure S2 for all components obtained from EEMD). We also omitted BOT components since it presented only one main mode of variability corresponding to 93.3% of the variance (C5 with averaged period of ~1h43 min; Supp. Figure S2e). The space- and timescale for this modulation trace back the cyclic change in depth due to the MRT transect repetition shown in **Figure 4f**, while the remaining components are representative of small-scale bottom features. The average period represented of C5 from BOT will be called here onwards as shelf-slope scale, that represents the variability related to shelf-ocean gradient.

Table 1. Variance (Var), averaged period (Period) and maximum amplitude (MA) for variability components with variance higher than 5% obtained from Ensemble Empirical Mode Decomposition (EEMD) of bottom depth (BOT), cross-shelf (CS-TIDE) and along-shelf (AS-TIDE) current from tidal model TPXO9, averaged cross-shelf (CS_{avg}) and along-shelf (AS_{avg}) velocities observed velocities during MRT survey.

Bottom depth (BOT)							
IMF	**Var (%)**	**Period**	**MA (m)**				
C5	93.3	1h43 min	457				
CS-TIDE				**AS-TIDE**			
IMF	**Var (%)**	**Period**	**MA ($m.s^{-1}$)**	**IMF**	**Var (%)**	**Period**	**MA ($m.s^{-1}$)**
C4	12.5	55min	0.014	**C4**	7.9	50min	0.041
C5	39.2	1h33min	0.02	**C5**	20.4	1h26min	0.033
C7	44.6	12h27min	0.013	**C7**	68.3	12h40min	0.038
CS_{avg} velocity				**AS_{avg} velocity**			
IMF	**Var (%)**	**Period**	**MA ($m.s^{-1}$)**	**IMF**	**Var (%)**	**Period**	**MA ($m.s^{-1}$)**
C4	10.2	43min	0.05	**C4**	21.5	50min	0.09
C5	67.7	1h25min	0.13	**C5**	26.6	1h37min	0.08
C8	5.1	12h24min	0.02	**C7**	44.4	12h39min	0.07

Preprint not peer reviewed

This preprint research paper has not been peer reviewed. Electronic copy available at: https://ssrn.com/abstract=4861987

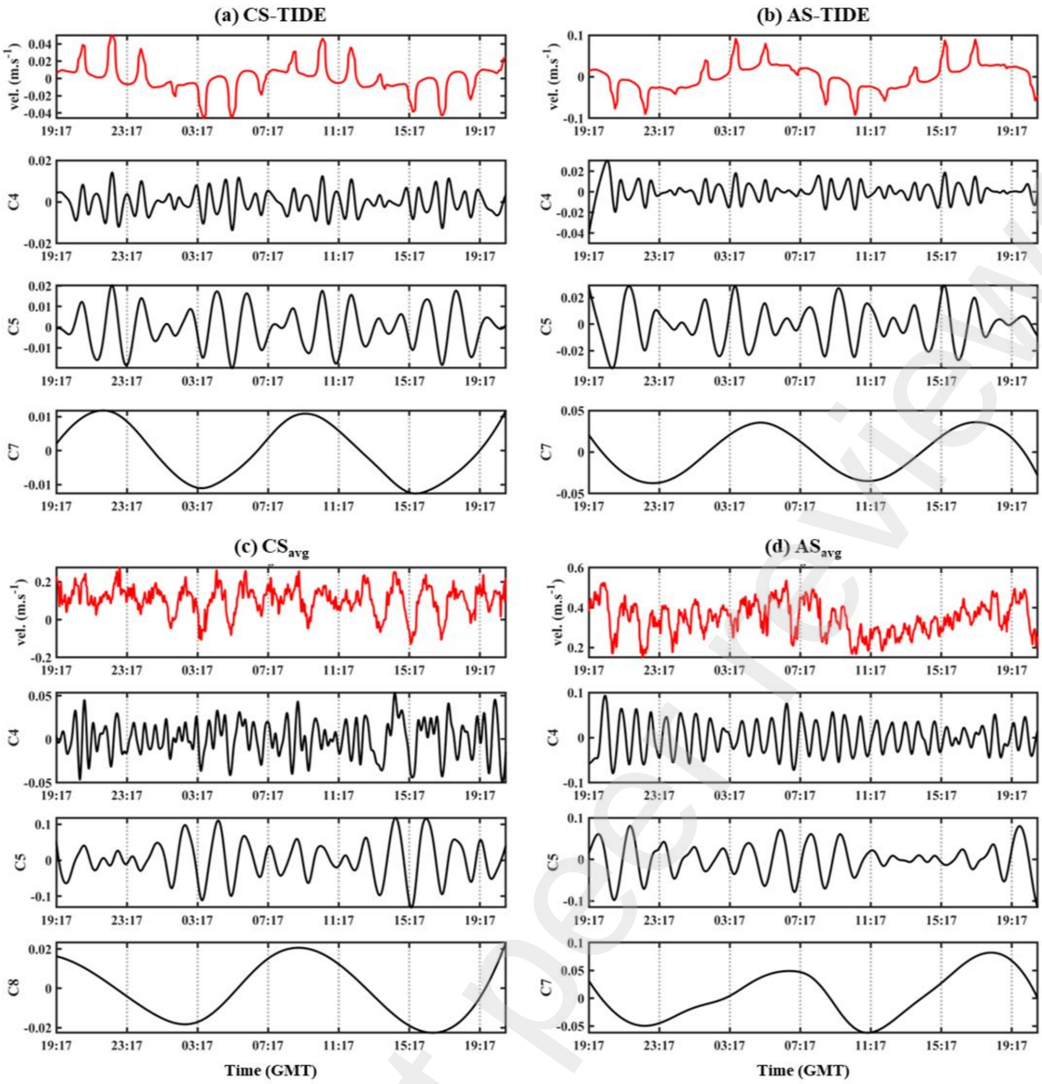

Figure 5. Main variability (highest variance) modes of (a) cross-shelf (CS-TIDE) and (b) along-shelf (AS-TIDE), (c) averaged cross-shelf (CS_{avg}) and (d) along-shelf (AS_{avg}) obtained through the EEMD method. The components C4, C5 and C7 were the most important for CS-TIDE, AS-TIDE and AS_{avg}, while the components C4, C5 and C8 were the main components for CS_{avg}. The original timeseries is presented for a comparison with the components as the red line on the top of (a) to (d). For the complete results of the EEMD method, see Figure S3 and S4.

The decomposition off the tidal current extracted from the tidal model TPXO9, CS-TIDE and AS-TIDE, highlighted three main variability modes C4, C5 and C7 (**Table 1**). For CS-TIDE and AS-TIDE, the most important variability scale was represented by C7 (avg. period of 12h27min and 12h40min), followed by C5 (avg. period of 1h33min and 1h26min) and C4 (avg. period of 55min and 50min). The period for C7 matches the expected period for semi-diurnal tidal forcing while the period for C5 is close to the period for the shelf-ocean scale. C4 matches the half of the period to achieve the one rectangle in the MRT experiment, however, it will not be discussed since it presented smaller variance and did not correlate with none of the observational data. The resulting patterns of both C5 and C7 will be used for a comparison with the CS_{avg} and AS_{avg} EEMD results further ahead.

For CS_{avg} and AS_{avg}, within our spatiotemporal framework, we depicted three main characteristic scales: (i) tidally forced variability (C7 and C8); (ii) shelf-ocean variability (C5); and (iii) shelf-break variability related to gradients that peak in the transition between the shelf and the slope. These scales are interrelated in the SBS across a variety of interacting processes, mostly due to the along-shelf dynamics and tidal forcing.

Preprint not peer reviewed

This preprint research paper has not been peer reviewed. Electronic copy available at: https://ssrn.com/abstract=4861987

(i) Semi-diurnal variability (C7, C8)

Semi-diurnal variability was depicted in mode C8 for CS_{avg} and C7 for AS_{avg} (averaged period of ~12h32min; **Table 1**) with contributions of 5.1% and 44.4%, respectively, of the total current variability observed during the MRT survey. Tidal forcing was inferred by the strong correlations (CI_{global} >0.8) between the modeled and observed semidiurnal cross-shelf (**Figure 6a,b**) and along-shelf components (**Figure 6c,d**). However, the observed cross-shelf and along-shelf amplitudes for the components were larger than the estimated by the tidal current model (0.02 vs. 0.013 $m.s^{-1}$/0.07 vs. 0.038 $m.s^{-1}$, respectively; **Table 1**).

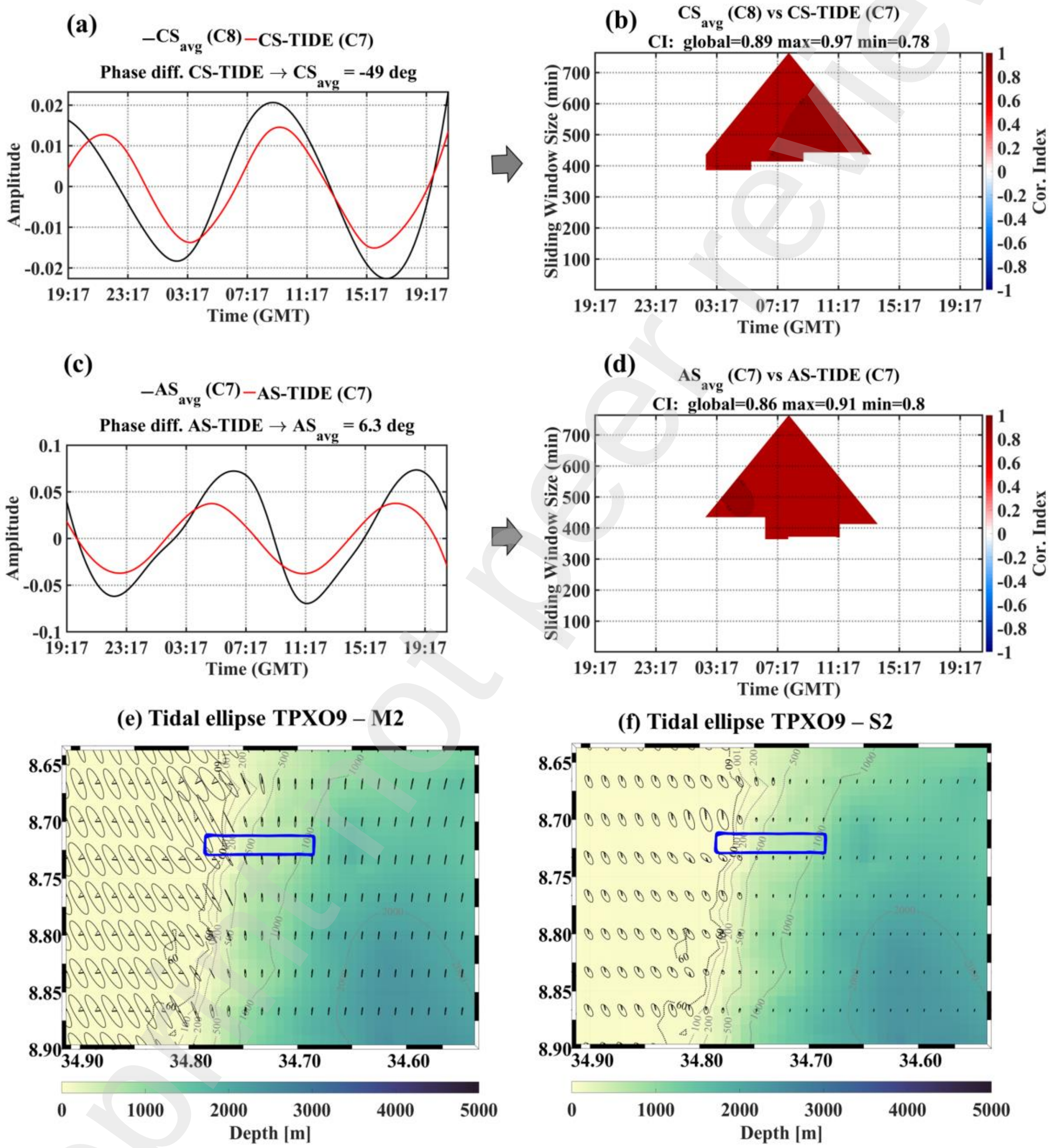

Figure 6. Intrinsic Mode Function C7 of CS-TIDE (black line) and C8 of the CS_{avg} $m.s^{-1}$ (red line) **(a)** and the resulting Time Dependent Intrinsic Correlation **(b).** Intrinsic Mode Function C7 of AS-TIDE (black line) and C7 of the AS_{avg} $m.s^{-1}$ (red line) **(c)** and the resulting correlation **(d)**. Tidal ellipses for the semidiurnal components **(e)** M2 and **(f)** S2 from TPXO9. Blue rectangle represents the location of the MRT.

In summary, the semi-diurnal components of the IMFs, from the observed shallow currents, shows that the tidal forcing is the responsible for the main variability observed in the along-shelf current, while it only represents a small fraction of the variability observed for the cross-shelf current. M_2 Tidal

Preprint not peer reviewed

This preprint research paper has not been peer reviewed. Electronic copy available at: https://ssrn.com/abstract=4861987

ellipses extracted from the tidal model TPXO9 (**Figure 6e,f**) shows that the main direction for tidal current in the MRT surroundings, is indeed the along-shelf direction. Additionally, those components have a period longer than the MRT scale and are therefore, independent of the measurement location (shelf or slope), which cannot be said about the higher frequency modes that will be visited in the next sections.

(ii) Shelf-slope variability (C5)

Current variability components with averaged period close to the shelf-slope scale (C5 of CS_{avg} and AS_{avg}, with period ~ 1h31min) are expected to be related to cross-shore features along the shelf-ocean gradient. Both observed cross-shelf and along-shelf presented timescales close to this scale, however with more contribution for the total current variability for the cross- than for the along-shelf, explaining 67.7% and 26.6% of the total variability, respectively. To investigate the shelf-slope patterns, we present superimposed of C5 from CS_{avg} and AS_{avg} and C5 from bottom-depth (**Figure 7a,c)** and the TDIC correlation between them (**Figure 7b,d)**.

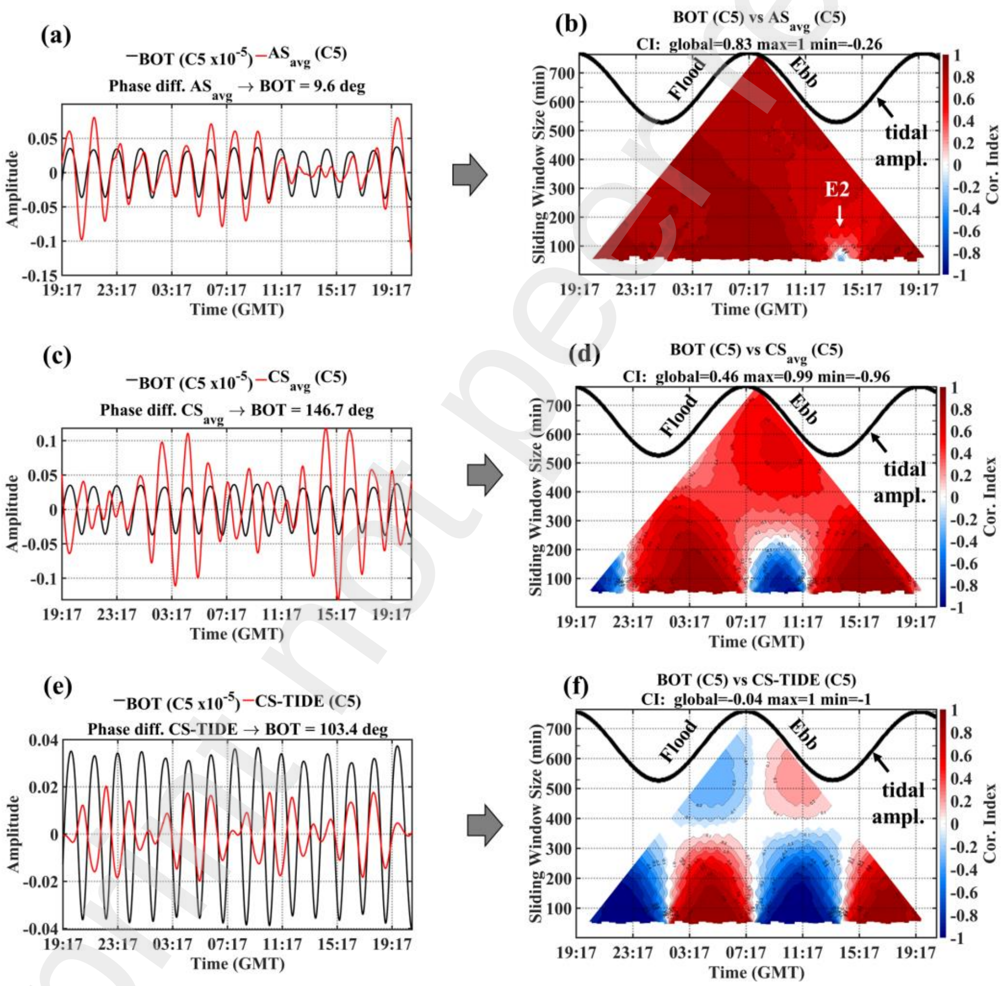

Figure 7. Intrinsic Mode Function C5 of BOT in m*10^{-5} (black line) and C5 of AS_{avg} **(a)**, CS_{avg} **(c)**, and CS-TIDE **(e)** in m.s^{-1} (red lines) and the respective correlations **(b)**, **(d)** and **(f)**. E2 in **(b)** highlight the change in correlation of the AS_{avg} with BOT. Tidal amplitude is presented at the top of the correlation results in **(b)**, **(d)**, **(f)** as reference for tidal moment (i.e., ebb/flood, low/high tide).

In the case of the along-shelf component, C5 mode was highly and mostly positively correlated with bottom-depth for almost all the survey timeframe (CI global: 0.77, max/min=1/-0.24; **Figure 7a,b**). Positive correlations between the BOT-C5 and along-shelf C5 indicate that stronger along-shelf currents

Preprint not peer reviewed

This preprint research paper has not been peer reviewed. Electronic copy available at: https://ssrn.com/abstract=4861987

were observed on the slope and weaker along-shelf currents are observed on the shelf, creating therefore, a stronger zonal gradient of the along-shelf current. This cross-shore gradient of the along-shelf current is expected due to the NBUC acting against the slope in this region (Hummels et al., 2015; Araujo et al., 2019; Dossa et al., 2021). However, the gradient seems to be increased during high tide, when compared to low tide (**Figure 7a**), which implicates that tidal forcing is increasing (decreasing) the along-shelf current on the slope (on the shelf) during the high tide, and the opposite happens during low tide. Indeed, during the second low tide, the shelf-slope gradient in AS_{avg} reversed (see Event E2 in **Figure 7b**).

The correlation between the mode C5 of CS_{avg} and bottom-depth was high but oscillated between in phase (maximum CI = 0.99) and out of phase (minimum CI = -0.97) (**Figure 7c,d**). Positive correlations between the BOT-C5 and cross-shelf C5 indicate that positive cross-shelf currents are observed on the slope and negative cross-shelf currents are observed on the shelf, creating a divergent pattern. The opposite is true for negative correlations, where the positive cross-shelf current on the shelf and negative on the slope simulates a convergent pattern. Correlation between CS-TIDE C5 with bottom depth (**Figure 7e,f** reproduce the same patterns as CS_{avg}, which lead us to conclude that tidal forcing is driving these cross-shore spatial patterns.

To illustrate, we present the predicted tidal current in our study region at two moments (**Figure 8c,d**) - flood and ebb, respectively - during the execution of the MRT. The results show negative values of the zonal current (positive meridional current) on the shelf and positive zonal current (weakly negative meridional current) on the slope during the flood and the opposite during the ebb. The co-tidal lines are also presented for M2 and S2 tidal constituents for the region (**Figure 8e-f**) and they explain why the tidal current have this shelf/off-shelf modulation. A large phase difference in a short distance on the MRT location can be observed from the cotidal lines that are almost parallel to the shelf break and slope isobaths (**Figure 8e,f**). In addition, the divergent/convergent patterns of the tidal current can be explained by the major semi-axis (i.e., the maximum tidal current velocity), that is almost northwestward on the shelf and northeastward on the ocean side (**Figure 6e,f**).

Nevertheless, the flood in the observed cross-shelf component is longer than in the tidal model prediction (local positive strong correlation in **Figure 7d-f**). This asymmetry between the ebb and flood is commonly observed at of narrow systems with strong tides and subjacent flows, manly in coastal systems such as tidal channels and estuaries. It can be related to non-linear interactions, inertia, tidal current interaction with bottom morphology, and/or the subjacent flows (e.g., Nidzieko and Ralston, 2012; Yoon and Woo, 2013; Guo et al., 2014; Li et al. 2016). To our knowledge tidal asymmetry was not reported before for the shelf-slope transition. Although we are discussing only one mode of variability, this mode represents more than 67% of the total current variability. This further highlights the importance of these findings since this asymmetry can have implications for the cross-shelf transport of sediments and nutrients.

In addition, the cross-shelf velocity observed during the MRT experiment is one magnitude order higher than the model estimates (maximum amplitude: observation/model =0.13/0.02 $m.s^{-1}$). This difference between model and observation can lead to two main inferences: (i) tidal model is highly underestimating the cross-shore current or (ii) another process is acting to increase cross-shelf exchanges. One evidence that points to the second option is the current horizontal gradient (i.e., horizontal shear) created by the faster along-shelf current in the oceanic side of the MRT – with additional tidal contribution during the flood – and slower current at the adjacent shelf. In some instances, the increased horizontal shear can lead to the generation of residual cross-shelf flow (Brink, 2016) that might account for the difference in model/observed cross-shelf current. We will revisit this possibility in section 3.3.

Preprint not peer reviewed

This preprint research paper has not been peer reviewed. Electronic copy available at: https://ssrn.com/abstract=4861987

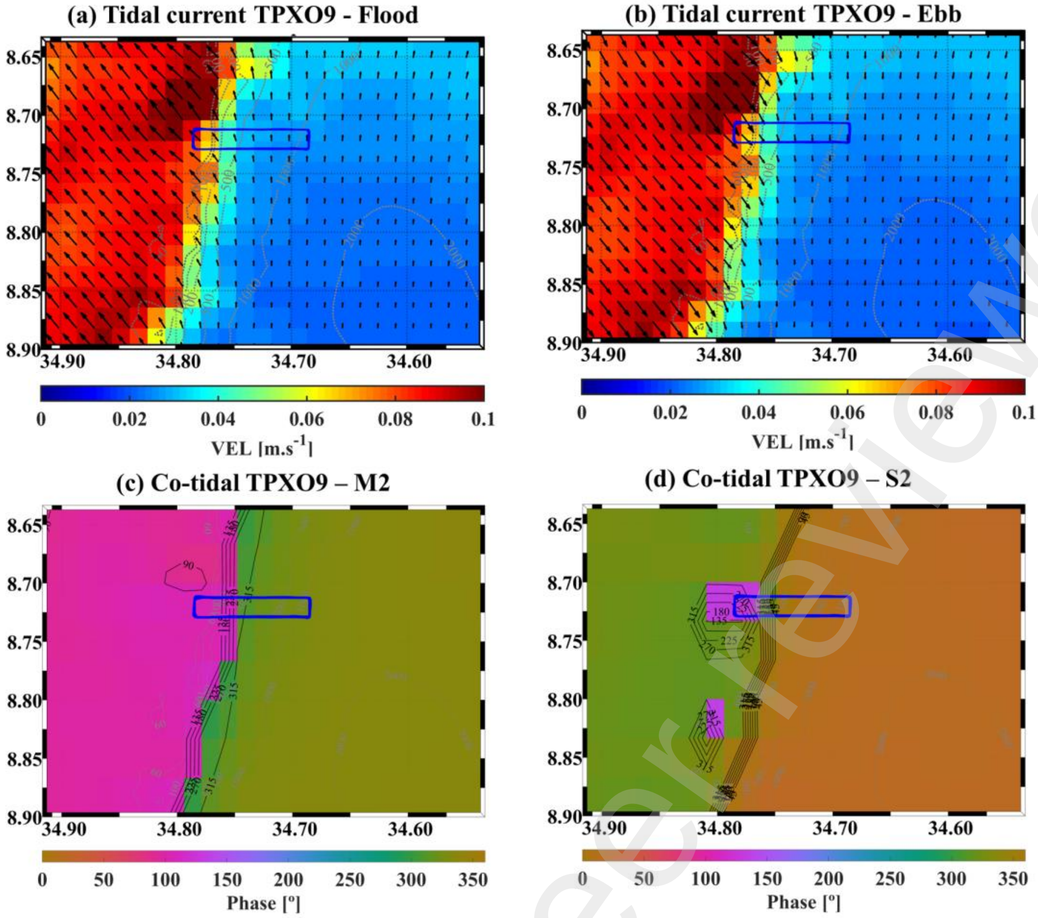

Figure 8. Tidal current velocity predicted from tidal model TPXO9 (Egbert and Erofeeva, 2002) at two moments – **(a)** flood and **(b)** ebb – during the execution of the multiple rectangles transect (MRT) experiment. Co-tidal (Phase) for the semidiurnal components **(c)** M2 and **(d)** S2 from TPXO9. Blue rectangle represents the location of the MRT.

(iii) Shelf-break variability (C4)

The scale of ~47 min was representative of shelf/shelf-break/slope variability, i.e., the features peak at the transition between the shallow and deeper waters. This scale was represented by the C4 component and contributed for 10.2% and 21.5% of the cross- and along shelf current total variability. The high variability for the along-shelf its related to the stronger along-shelf current near the shelf-break limit. In our case, this scale evidence a stronger current in the region closest to the slope wall than on de adjacent shelf and ocean (**Figure 9a**). Interestingly, like shelf-slope scale (AS_{avg} C5), the C4 scale, was also influenced by the tide, as illustrated by the intensification of the shelf/shelf-break/slope patterns during the high tide (**Figure 9b**).

Preprint not peer reviewed

This preprint research paper has not been peer reviewed. Electronic copy available at: https://ssrn.com/abstract=4861987

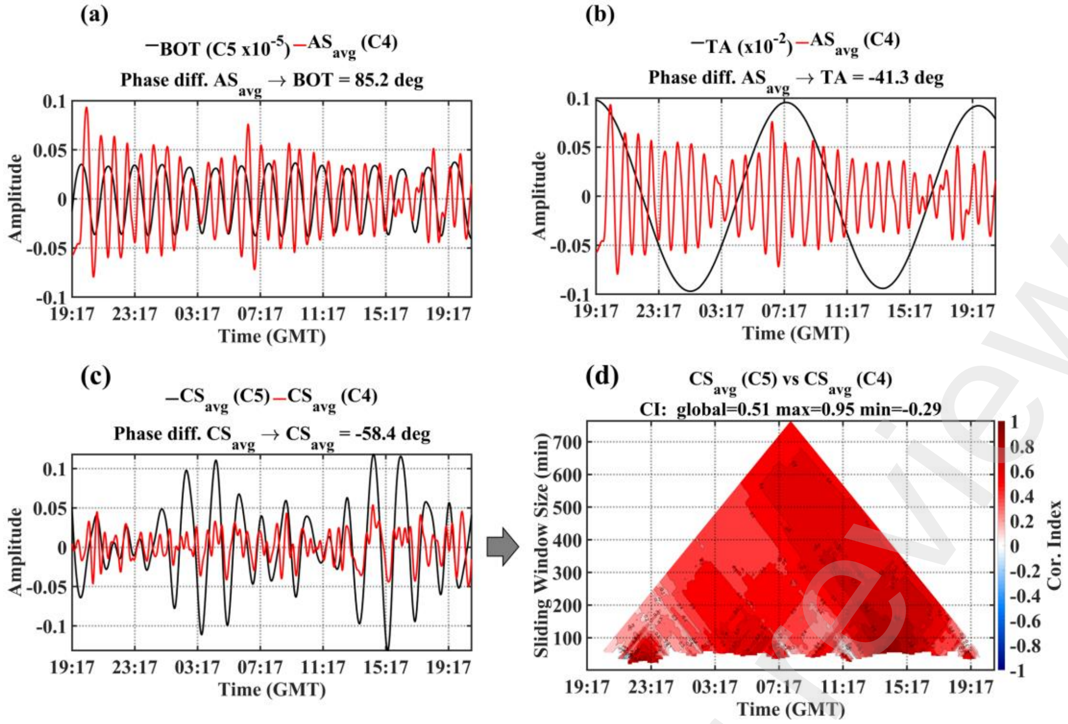

Figure 9. Intrinsic Mode Function C4 of AS_{avg} in m.s^{-1} (red line) superimposed to C5 of BOT in m*10^{-5} **(a)** and the tidal amplitude in m*10^{-2} **(b)** (black lines). Intrinsic Mode Function C5 (black line) and C4 (red lind) of CS_{avg} **(c)** and the resulting correlation **(d)**.

The cross-shelf component C4 did not present discernible shelf-break patterns. Nonetheless, TDIC results of this mode with the lower frequency mode C5 showed moments of high local correlation, mostly around 12:50 and 15:47 GMT (**Figure 9c,d**), when both cross-shelf C5 and C4 amplitudes were higher. The timing for this correlation matched the event E1 for the along-shelf component C5 when the shelf/ocean gradient reversed. Although we cannot be sure due to the short timeframe for the MRT transects, that might indicate non-linear interaction of the along-shelf and with cross-shelf currents through horizontal shear.

3.3 Tidal contributions to shelf break dynamics

As pointed by Brink (2016), little is known about the general cross-shelf flow components and mechanisms, due to their complexity and variability in time and space. During the MRT experiment, at the shelf-break/slope transition, we observed cross-shelf current alternation between shelf-ward and ocean-ward current. **Figure 10a** presents snapshots of the cross-shelf current during the flood (left panel) and ebb (right panel) registered during the MRT experiment. In the flood, the current was shelf-ward over the shelf but ocean-ward over the slope, creating a divergent pattern. Oppositely, during the ebb, the flow was shelf-ward over the slope and ocean-ward over the shelf and shelf-break, creating a convergent pattern. The current variability observed in those patterns was captured as the main variability component C5, of the cross-shelf current (**Figure 7c**).

Although wind is a known driver of shelf-break dynamics (Allen, 1980; Lentz, 2001; Lentz and Chapman, 2004), when the wind is weak, as in our case, other processes be responsible for the cross-shelf patterns (Brink, 2016; Dever, 1997; Schaeffer et al., 2013). Shelf-ward transport can also be induced by IWs propagation (Pineda, 1994, Cacchione, 2002; Lamb, 2013). When analyzing the cross-shelf flow to search for IW propagation across the shelf-break in shallow layers, our results pointed to internal tidal waves (CS_{avg} mode C7). However, this component did not present significant variability

Preprint not peer reviewed

This preprint research paper has not been peer reviewed. Electronic copy available at: https://ssrn.com/abstract=4861987

(<5% of variance, **Table 1**). Therefore, IW dynamics was likely not the major contributor to the cross-shelf transport of the cold and salty waters that reached the shelf. Baroclinic instabilities can also create cross-shelf exchanges, due to horizontal density gradient compensation in shelf-break frontal dynamics (Barth et al., 1998; Cottier et al., 2005). Nevertheless, although the surface cross-shelf velocity variability resemble a shelf-break front at times, sea surface temperature and salinity gradients were too small (amplitude of 0.73°C for SST and 0.25 for SSS, **Figure 4b,c**) to be considered as fronts. The same can be said about undersurface temperature and salinity from CTD and XBT that do not present horizontal gradients as marked as those expected in frontal systems (Yanagi, 1987; Barth et al., 1998; Acha et al., 2004).

As we commented in Section 3.2(ii), the tidal forcing is likely the main driver of these cross-shelf patterns, since the same patterns were observed from the cross-shelf velocity from the tidal model (CS-TIDE C5 variability, **Figure 7e**). In the tidal model, the cross-shore variability seems to arise from the phase difference between the slope and the shelf-break (**Figure 8c,d**). This phase difference is known to result from bottom friction over changing bathymetry (e.g., Huthnance, 1973; Stern and Shen 1976; Loder, 1980; Loder and Wright 1985) or, in the absence of bottom friction, from if nonlinear effects (Robinson, 1981). The tides also play a role in changing along-shelf dynamics, which can be observed by the tidal influence beyond the semidiurnal component (C7), on the higher-frequency variability modes (C4 and C5) registered during the MRT experiment. To illustrate the tidal influence in both, along- and cross-shelf currents we present the Hilbert spectrum (HS) for the IMFs obtained by post-processing the results from the EEMD for AS_{avg} and CS_{avg} (**Figure 10b**). The spectrum represents the energy as the square of the amplitude in the time-frequency domain. Energy for the along-shelf velocity HS peaks at high tide at different frequencies in (left panel) compared with the tidal amplitude extracted from TPXO9 (left-bottom). Energy for the cross-shelf velocity (right) is higher centered around 90min (i.e. at the cross-shore scale) and only decreases when the C7 component of AS_{avg} is at his minimum (right-bottom). As we explained in section 3.2(i), the C7 component of the AS_{avg} is related to the semi-diurnal tidal forcing.

The general conclusion here is that the tidal forcing increased the energy of the along-shelf current across the timescales. In turn, this energy is transferred from the along-shelf current to the cross-shelf component, increasing the gradients of the observed cross-shelf ebb/flood patterns (**Figure 10a)** in relation to the predicted by the tidal model. Indeed, the tendency of stronger along-shelf velocity at the shelf-break transition than over the surrounding shelf and oceanic waters can create zonal compensating fluxes (i.e., divergence in the zonal direction) (Matano and Palma, 2008). Additionally, this might explain why the cross-shelf current variability, observed during the MRT experiment was one order magnitude higher than the tidal model prediction. Snapshots of the along-shelf current recorded during the MRT experiment (**Figure 10c**) shows that the horizontal gradient of the current on the shelf and the slope was stronger during the high tide (left panel) and weaker during low tide (right panel).

Preprint not peer reviewed

This preprint research paper has not been peer reviewed. Electronic copy available at: https://ssrn.com/abstract=4861987

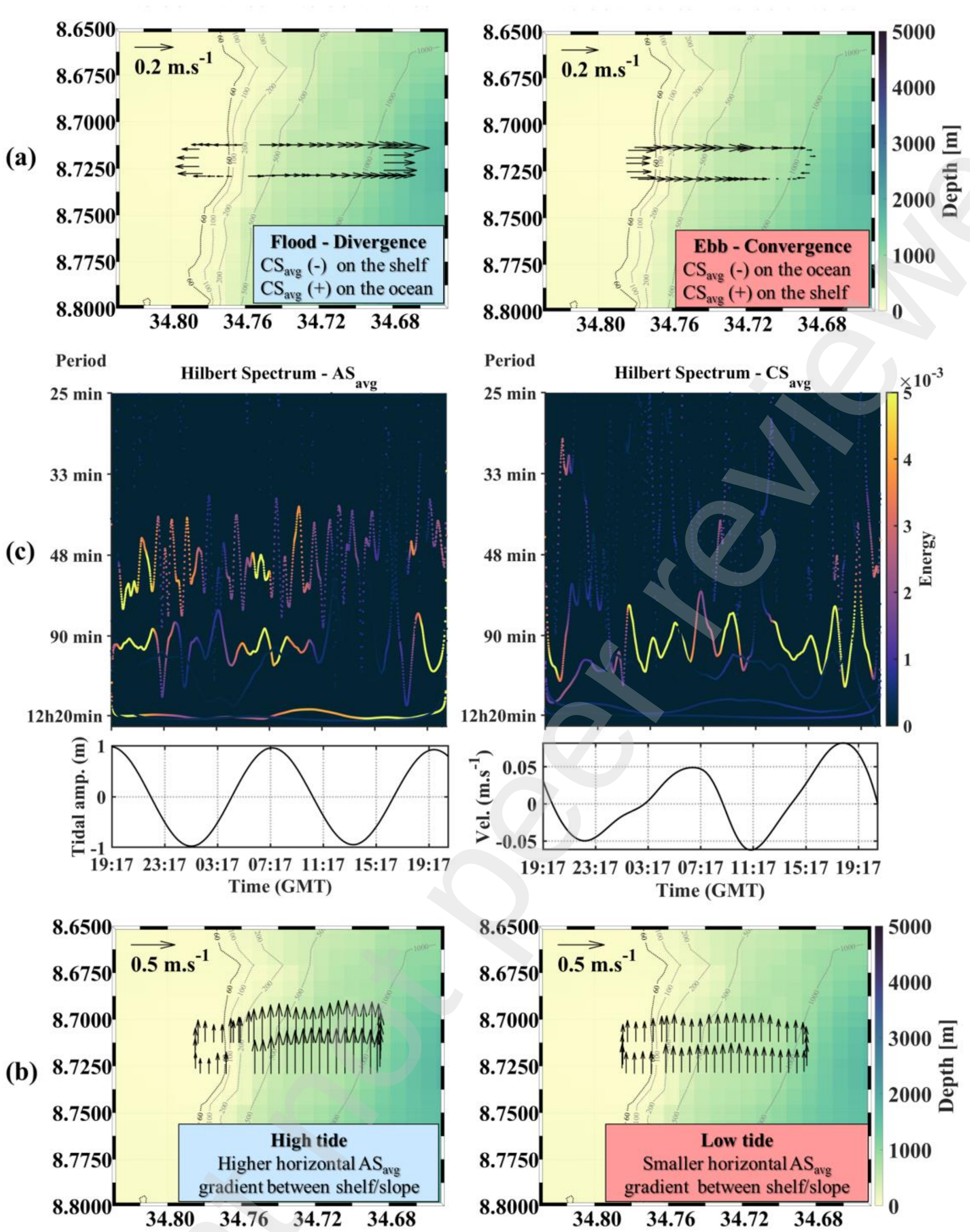

Figure 10. (a) Hilbert Spectrum for the IMFs of AS_{avg} (from reprocessed EEMD) and Tidal amplitude extracted from TPXO9-atlas for the same period and location (left) and; Hilbert Spectrum for the IMFs of CS_{avg} (from reprocessed EEMD) and C7 from AS_{avg} (semidiurnal component) for the same period and location (right). Snapshots of the MRT current (arrows) at highlighted moments of **(b)** the cross-shelf current during flood/ebb (divergence/convergence), on the left and right, respectively; and **(c)** along-shelf current during high/low tide (high/low horizontal shear).

Considering that the tides affect the dynamics in the shelf break transition in our study region, we should expect it to also affect uplift variability. The uplift in the Southwestern Tropical Atlantic region was firstly reported by Silva et al. (2021) and, although they did not propose a mechanism for such observation, it was mentioned that the NBUC was mostly likely the main forcing. The uplift can be observed by the tilting of the isotherms to shallower depths closer to the slope, as we observed from the climatology (**Figure 3i**) and the St. 2 in relation to St. 6 (**Figure 3c**). In addition, NBUC seasonality includes the shallowing of the upper limit of the NBUC (**Figure 3k,l**), which should change the

Preprint not peer reviewed

This preprint research paper has not been peer reviewed. Electronic copy available at: https://ssrn.com/abstract=4861987

interaction of this current with the shelf dynamics and therefore, the intensity of the uplift. From the regional context, climatology indicates stronger uplift, and tendency to upwelling in austral winter (**Figure 3j**) when the NBUC is shallower and stronger (**Figure 3l**).

During the fall of 2017, the context of our MRT experiment, the NBUC core was shallow (Dossa et al., 2021), which also allows for the interaction with coastal currents dynamics that generate uplift. As we presented in this work, the tides play a role in changing the NBUC shallow dynamics, therefore, we should expect this to have some implications for uplift variability in a small timescale (within a tidal cycle). The uplift should increase at high tide, led by the intensification of the along-shelf velocity in subsurface and decrease during low tide, with de decrease of the along-shelf velocity. If indeed that is the case, it should explain why, at the local scale, not all stations presented marked uplift (**Figure 3c,h**). As expected, the uplift was stronger at high than low tide (see X5 at high tide vs. X1 at low tide in **Figure 3h)**, however, the isotherm configuration during high tide agrees with the climatological patterns (**Figure 3g,h**). This indicates that the tidal forcing during high tide is not increasing uplift in relation to climatological patterns, but tidal forcing during low tide is in fact decreasing uplift.

Nevertheless, another important implication of the tides to uplift variability, arises from the cross-shelf current patterns during the flood. During the flood, the shelf-ward flow can transport uplifted water towards the shelf-break, as seems to be the case for St. 8 (**Figure 3c**), that was performed during the end of the ebb period in the high tide. The uplift, followed by the periodic supply of richer waters to the shelf-break region can have important implications for primary production within tidal cycles, as evidenced by the increase in chlorophyll-a in St. 8 (**Figure 3d**), even with a modest associated decrease in temperature. The contribution of sub superficial slope water can have implications for primary productivity, as the inferior limit of the euphotic layer in the northeast Brazil can reach down to 60-90 m, outside the influence of major rivers flows (Macedo et al., 2009). In addition, it can have cascade effects for top-predators (and fisheries) through bottom-up structuring (Bertrand, 2008b; 2014), favoring the shelf-break/slope region. Indeed, despite being previously classified as oligotrophic (Ekau and Knoppers, 1999; Araujo et al., 2019), Eduardo *et al.* (2018) showed that fish diversity and abundance in Northeast Brazilian waters were higher than expected. They observed areas of high fish densities and diversity near the shelf-break, between 30 and 60 m of depth. The cross-shelf flow contribution to the transport of enriched waters towards the shelf could explain why the areas of high fish densities and diversity are located close to the shelf-break. In addition to that, the turbulence generated by the horizontal gradient of the along-shelf current can generate shear, that is known to mix and reorganize the tracers (e.g. nutrients) and planktonic organisms in the water column (Denman and Gargett, 1983; Haury et al., 1990; Bertrand et al., 2008b).

Finally, the interaction of the western boundary current NBUC with the tides – represented by the increase of amplitude in all three main modes of the along-shelf current during high tide – and the resulting cross-shelf velocity, points out to important tidal contributions to shelf-edge exchanges in this region. Since the NBUC is part of the upper AMOC, these exchanges are of topical interest for global fluxes, budgets and their response to climate change and human activities (Huthnance, 1995). Additionally, anomalous variability in the cross-shelf exchanges, can indicate changes in dynamics of the adjacent WBC (Gawarkiewicz et al., 2018; Todd et al., 2019), which justify the need for high-resolution long-term observation here and in other WBC systems.

Preprint not peer reviewed

This preprint research paper has not been peer reviewed. Electronic copy available at: https://ssrn.com/abstract=4861987

4. Summary and final considerations

In this work, we investigated the high-frequency variability of shelf-break/slope dynamics and the influence on uplift variability in a western boundary system in the Southwestern Tropical Atlantic. The western boundary current in the system was the North Brazil Undercurrent (NBUC) and the high-frequency variability was depicted through adaptative signal analysis of the continuous data obtained during the Multiple Rectangles Transect experiment. Additionally, in situ profiles and regional climatological data provided the needed framework to give a comprehensive characterization of the termohaline structure setting and investigate uplift variability.

Tidal forcing was the main responsible for the observed variability of the along- and cross-shelf currents. Local variability of uplift intensity was also related to tidal forcing. The tidal currents interact with the subjacent flow of the NBUC, decreasing uplift during low tide. Additionally, tidal forcing creates alternating divergent/convergent moments during flood/ebb; and flood timing for cross-shelf flow can enhance tracer transport toward the shelf. This can have important implications for transport and mixing of nutrients, and therefore primary production, within a tidal cycle. In summary, the tidal forcing observed during the MRT survey seems to contribute for shelf-break/slope dynamics and uplift variability in different scales. In this manner, tidal forcing appears as an important process to be considered in uplift mechanisms for the western boundary system in question. The NBUC core also shows seasonal vertical displacements that might affect the uplift intensity of colder waters. Therefore, seasonal core depth and tidal forcing needs thus to be considered when disentangling upwelling/uplift mechanisms in Northeast Brazilian waters in future research.

We highlight the potential of the multiple rectangles transect observing strategy together with the adaptive analysis that provided novel information about the shelf-break/slope dynamics. The importance of the adaptive analysis lies in the explicit consideration that relationships in natural data change with time at different scales. This was exemplified in our results by the low global correlation index, compared with the high correlation and anti-correlation, in smaller windows sizes between bottom-depth and cross-shelf velocity. Any other stationary method would not be able to present such clear correlation results.

In what concerns the Multiple Rectangles Transect experiment, although it is a feasible, low cost – when compared with the high cost of mooring – method to obtain timeseries from oceanographic variables; there are many limitations. Two of them are the short timeframe of observations and the need for simultaneous water termohaline structure, that limits the inferences in this work. From our experience, we concluded that the MRT experiments should have at least 48h of duration if the aim is to further investigate tidal effect on current dynamics. Additionally, it should benefit greatly from underway measurements of the vertical stratification, such as those obtained through underway CTD profilers. Continuous cross-shelf sections with underway CTD measurements should give a better insight of the thermohaline and dynamical structure during the experiments.

Lastly, as the region is important for the Atlantic Meridional Overturning Circulation, investigations are still being conducted to understand and quantify the influence of the tides in the WBS in the SWTA and the uplift mechanisms using high resolution modelling. And, although regions of elevated bathymetric gradients are recognized as hot spots for productivity, there still need to investigate how the processes observed here really contribute to enhance biological productivity on the Northeast Brazilian waters, e.g., if nutrient residence time in the slope is reduce due to the high transport of the along shelf current.

5. Data Availability

Preprint not peer reviewed

This preprint research paper has not been peer reviewed. Electronic copy available at: https://ssrn.com/abstract=4861987

The quality controlled CTD datasets are freely available at SEANOE repository (https://doi.org/10.17882/76352). The quality-controlled sea surface temperature and salinity, raw current velocity, wind, XBT and echosounder bathymetric data obtained during the MRT experiment is available through request to the LMI-TAPIOCA/IRD principal investigator (arnaud.bertrand@ird.fr). CMEMS reanalysis product is freely available at the Copernicus Marine Service database (https://doi.org/10.48670/moi-00021).

Appendix 1 - Ensemble Empirical Mode Decomposition and Time Dependent Intrinsic Correlation

To introduce the Ensemble Empirical Mode Decomposition method, one must first understand the Hilbert Huang Transform (HHT) and the Empirical Mode Decomposition (EMD), as both methods are linked to the development of the EEMD. Time-series of natural data usually present non-linear and non-stationary characteristics, which are not well represented by most traditional time-series analysis (e.g. Fourier Transform and wavelet) that are based on linear and/or stationary assumptions (Franzke, 2009; Huang and Schmitt, 2014; Kbaier et al., 2016). HHT – due to the *a posteriori* adaptive prerogative – allows both non-stationarity and non-linearity of the data. The HHT can give a full energy–frequency–time distribution of the data, the Hilbert spectrum, which is ideal for nonlinear and non-stationary data analysis (Huang *et al.*, 1998).

The development of the HHT was driven by the need to describe nonlinear waves in detail and its natural variations, common to nonstationary processes (Huang *et al.*, 1996; Huang *et al.*, 1998; Huang and Shen, 2014). One of the typical characteristics of nonlinear processes is their intra-wave frequency modulation, where the instantaneous frequency changes within one oscillation cycle (Huang *et al.*, 1998; Huang and Shen, 2014). Any deformation from the simple sinusoidal form wave-profile implies the intra-wave frequency modulation (Huang *et al.*, 1998). When using Fourier analysis, this intra-wave frequency can only be depicted by resorting to harmonics, and they appear as “harmonic distortions”. Those harmonic distortions lack physical meaning, as they are a mathematical artefact from imposing a linear structure on a nonlinear system (Huang *et al.*, 1998; 1999). To reveal the physical meaning and the intra-wave frequency modulations the analysis method requires the system description in terms of the instantaneous frequency (IF). Physically, there is also a real need for IF in a faithful representation of underlying mechanisms for data from nonstationary and nonlinear processes.

For non-stationary signals there are two main approaches to compute the instantaneous frequency, the quadrature method, and the analytic signal method (Cohen, 1995; Huang *et al.*, 2009). The first consists in directly computing the quadrature, a simple 90° shift of phase angle, and the latter can be obtained through the Hilbert spectral analysis (Huang *et al*., 2009). The Hilbert spectral analysis consists in applying the Hilbert transform (HT) to compute the instantaneous frequency of signals. After performing the HT, the data can be expressed in the time-frequency-energy domain. There are many applications of the Hilbert spectral analysis in the literature, such as theoretical mechanics, geophysics, and signal processing (Huang *et al.*, 1996). The Hilbert Huang transform, as denominated by the NASA, is a combination of the Hilbert Spectral Analysis and the Empirical Mode Decomposition (Huang *et al.*, 1996, 1998, 1999). In this method the instantaneous frequency is computed by applying the Hilbert transform to the Intrinsic Mode Functions (IMFs) resulting from the Empirical Mode Decomposition.

EMD is an adaptive *a posteriori* empirical analysis that accommodates the characteristics of non-linear and non-stationary data to separate the coexisting variability scales in any signal or time series. As well as in empirical orthogonal function (EOF) analysis, it is a decomposition of a signal into

Preprint not peer reviewed

This preprint research paper has not been peer reviewed. Electronic copy available at: https://ssrn.com/abstract=4861987

functions, in this case the IMFs, which are determined from the data itself. The method is analogous to performing principal components analysis on the data, except that the EMD returns temporal projections of the functions. Each variability component from the EMD is defined as an Intrinsic Mode Function that satisfies the following conditions: (1) across the entire data set, the number of extremes and the number of points crossing zero must be equal or at most, different by one and (2) at any point in the IMF, the average value of the envelope defined using local maxima and the envelope defined using local minima is zero (Huang *et al.*, 1998).

We present in **Figure A1a** a generic time-series of sea surface temperature $x(t)$. The IMFs are obtained through an iterative process that begins with the identification of the local extremes (maximum and minimum) of the signal. The local maxima (minima) are connected by a spline to form the upper (lower) envelope of the function (red lines in **Figure A1b**). Then, we obtain the average function of this envelope (m_1) (blue line in **Figure A1b**). The difference between the original signal $x(t)$ and the average function of this envelope (m_1) is called the first proto mode h_1 (**Eq. A1**).

$$h_1 = x(t) - m_1 \qquad (\boldsymbol{Eq. A1})$$

The process is repeated (sifting process) until the remaining signal meets conditions of an IMF presented above. I.e., the proto mode h_1 is treated as the data in the following iteration (**Eq. A2**).

$$h_1 - m_{11} = h_{11} \qquad (\boldsymbol{Eq. A2})$$

After k iterations (**Eq. A3**), h_{1k} becomes the first IMF, c_1 (**Eq. A4**).

$$h_{1(k-1)} - m_{1k} = h_{1k} \qquad (\boldsymbol{Eq. A3})$$

$$c_1 = h_{1k} \qquad (\boldsymbol{Eq. A4})$$

The sifting separates the finest local mode from the data based only on the characteristic time scale. However, this can have two effects: (a) the elimination of riding waves; and (b) the smoothing of uneven amplitudes. The first is necessary for the instantaneous frequency to be meaningful, and the second is also necessary in case the neighboring wave amplitudes have too large a disparity. Nonetheless, performing sifting the process to an extreme could make the resulting IMF a pure frequency modulated signal of constant amplitude, eliminating the physically meaningful amplitude fluctuations (Huang *et al.*, 1998).

Preprint not peer reviewed

This preprint research paper has not been peer reviewed. Electronic copy available at: https://ssrn.com/abstract=4861987

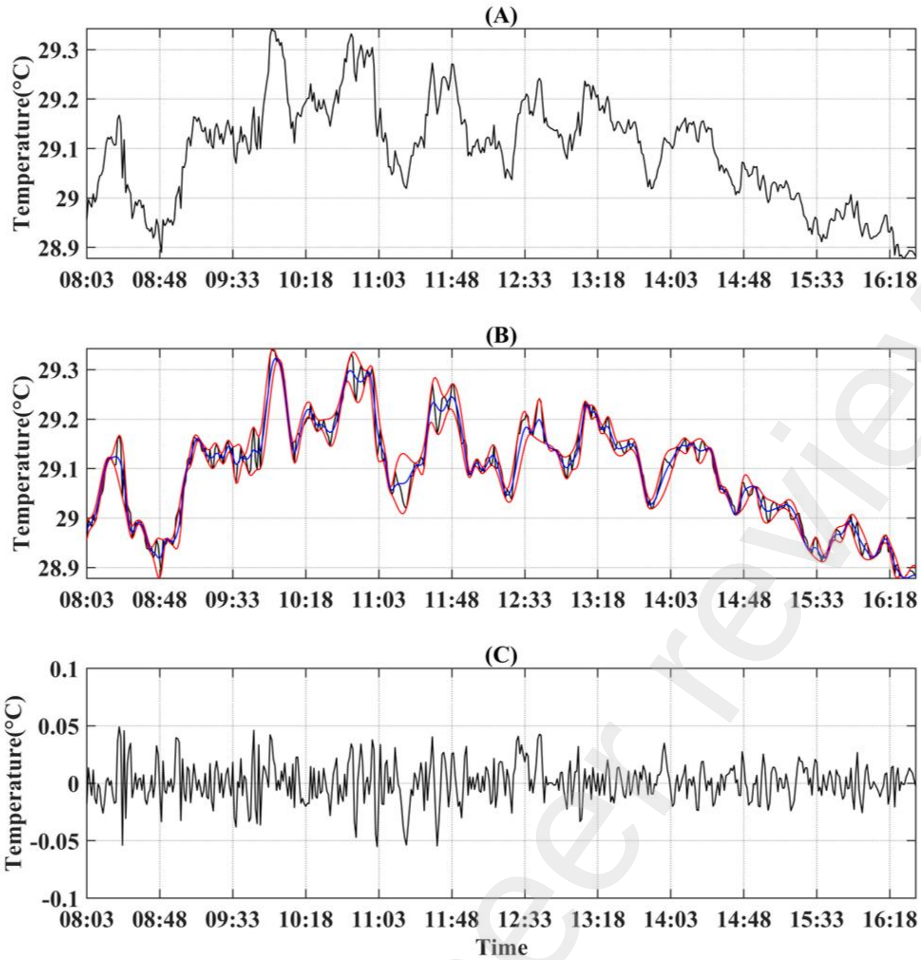

Figure A1. Illustration of the sifting processes: (A) the original data, x(t); (B) the original data (black line), with the upper and lower envelopes (red lines) and the mean, m_1 (blue line); (C) h_1, the difference between x(t) and m_1. h_1 is still not an IMF, for there are still negative local maxima and positive local minima suggesting riding waves.

To guarantee that the IMF components retain enough physical sense of both amplitude and frequency modulations, Huang *et al.* (1998) determined a criterion for the sifting process to stop. This criterion can be achieved by limiting the size of the standard deviation, SD, computed from the two consecutive sifting results, the same as the Cauchy's convergence criterion (**Eq. A5**). A typical value for SD can be set between 0.2 and 0.3.

$$\mathrm{SD} = \sum_{t=0}^{T}\left[\frac{\left|h_{1(k-1)}(t) - h_{1k}(t)\right|^2}{h_{1(k-1)}^2(t)}\right] \qquad (\boldsymbol{Eq.A5})$$

After the convergence criterion is reached, c_1 should contain the finest scale or the shortest period component of the signal. We can then separate c_1 from the rest of the data by **Eq. A6**.

$$x(t) - c_1 = r_1 \qquad (\boldsymbol{Eq.A6})$$

Now r_1 is the residue that still contains information of longer period components. It is treated as the new data and subjected to the same sifting process described above. This procedure can be repeated on all the subsequent r_j, and the result is:

Preprint not peer reviewed

This preprint research paper has not been peer reviewed. Electronic copy available at: https://ssrn.com/abstract=4861987

$$r_1 - c_2 = r_2, \ldots, r_{n-1} - c_n = r_n \qquad (\boldsymbol{Eq. A7})$$

The iteration can be stopped by any of the following predetermined criteria: either (a) when the component, c_n, or the residue, r_n, becomes so small that it is less than the predetermined value of substantial consequence, or (b) when the residue, r_n, becomes a monotonic function from which no more IMFs can be extracted. Even for data with zero mean, the final residue can still be different from zero; for data with a trend, then the final residue should be that trend. By summing up **Eq. A6** and **Eq. A7**, we finally obtain **Eq. A8.** Thus, we achieved a decomposition of the data into n-empirical modes, and a residue, r_n, which can be either the mean trend or a constant.

$$x(t) = \sum_{i=1}^{n} c_i - r_n \qquad (\boldsymbol{Eq. A8})$$

The **Figure A2a** shows the sea surface salinity recorded during the MRT experiment (top panel) followed by the results of the EMD decomposition in terms of the IMFs (C1 to C5) and the residue (bottom panel). The IMFs represent the different intrinsic timescales at which the original signal is modulated from the highest to the lowest frequency. The results should present a general separation of the data into locally non-overlapping time scale components. However, in this example we observe one of the major drawbacks of the EMD, that is the mode mixing, which is defined as a single IMF either consisting of signals of widely disparate scales, or a signal of a similar scale observed in different IMF components (Wu and Huang, 2009). From the MRT experiment we know that the main variability of the salinity is due to the change in the position of the measurements (shelf/slope). This is clear until 02:17, however, after this time, there are other scale processes overlapping the shelf-slope scale. That is the case for mode C3 and C4 (**Figure A2a**), there are similar scales in both modes. To reduce the mode mixing, we applied the Ensemble EMD (the EEMD) for the same time-series of sea surface salinity. The results (**Figure A2b)** show the improvement of variability modes separation, and now the shelf-slope scale was well represented in C5.

The Ensemble EMD (EEMD) was formulated by Wu and Huang (2009) to decrease the mode mixing drawback. It is based on the EMD with the additional application of the *Noise Assisted Data Analysis* (NADA). In this method we add a white Gaussian noise $w_n(t)$ to the original data $x(t)$ as in **Eq. A9** and then decompose the noise data $x_n(t)$ with the standard EMD. We perform several (N) trials with varying noise ensembles $w_n(t)$.

$$x_n(t) = x(t) + w_n(t) \qquad (\boldsymbol{Eq.\ A9})$$

At the end of the trials, the final IMFs are the ensemble mean of the trials resulting IMFs **Eq. A10**. In this manner, with enough number of trials, statistically, the added noise cancels out in the ensemble result.

$$imf(t) = \frac{1}{N}\sum_{n=1}^{N} imf_n(t) \qquad (\boldsymbol{Eq.\ A10})$$

Preprint not peer reviewed

This preprint research paper has not been peer reviewed. Electronic copy available at: https://ssrn.com/abstract=4861987

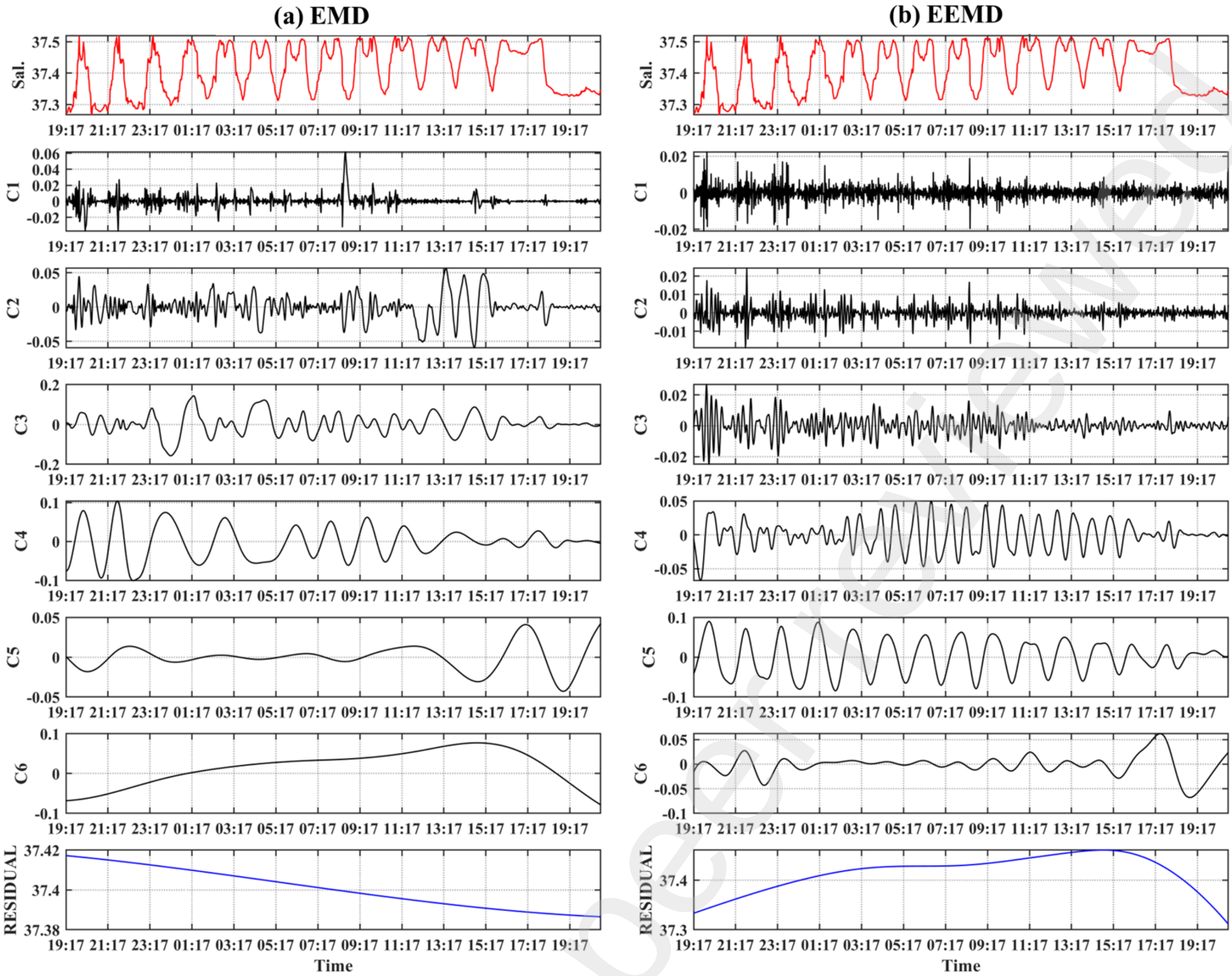

Figure A2. Results from the EMD for the wind speed data series presented in **Figure A1**. At the top is the original timeseries (red line), followed by the IMFs (C1 to C5) and the residual (blue line) or in this case, the trend at the bottom.

In EEMD, the number of ensemble and the noise amplitude are the two parameters that need to be prescribed. Wu and Huang (2009) recommend an ensemble number of a few hundred and a noise of an amplitude that is about 0.2 standard deviation of that of the data. However, when the data is dominated by high-frequency signals, the noise amplitude may be smaller, and when the data is dominated by low-frequency signals, the noise amplitude may be increased.

After the verification that the components extracted from the EEMD are IMFs (Wu and Huang, 2009), the physical meaning of the decomposition can be obtained through the Hilbert spectrum. That can be achieved by applying the Hilbert transform to the IMFs. For any function $x(t)$ of L^p class, its Hilbert transform $y(t)$ is given by the **Eq. A11** where P is the Cauchy principal value of the singular integral.

$$y(t) = \frac{1}{\pi} P \int_{-\infty}^{\infty} \frac{x(\tau)}{t-\tau}\, d\tau \qquad (\boldsymbol{Eq. A11})$$

With the Hilbert transform $y(t)$ of the function $x(t)$, we obtain the analytic function,

$$z(t) = x(t) + iy(t) = a(t)e^{i\theta(t)}\,, \qquad (\boldsymbol{Eq.\ A12})$$

where $i = \sqrt{-1}$,

Preprint not peer reviewed

This preprint research paper has not been peer reviewed. Electronic copy available at: https://ssrn.com/abstract=4861987

$$a(t) = (x^2 + y^2)^{1/2}, \qquad \theta(t) = tan^{-1}\frac{y}{x}. \qquad \textbf{(Eq. A13)}$$

Here a is the instantaneous amplitude, and θ is the instantaneous phase function. The instantaneous frequency is given by the **Eq. A14.**

$$\omega = \frac{d\theta}{dt} \qquad \textbf{(Eq. A14)}$$

With both amplitude and frequency being a function of time, we can express the amplitude (or energy, the square of amplitude) in terms of a function of time and frequency, $H(\omega, t)$.The marginal spectrum can then be defined by the **Eq. A15** where $[0, T]$ is the temporal domain within which the data is defined.

$$h(\omega) = \int_0^T H(\omega, t)dt, \qquad \textbf{(Eq. A15)}$$

The marginal spectrum represents the accumulated amplitude (energy) over the entire data span in a probabilistic sense and offers a measure of the total amplitude (or energy) contribution from each frequency value, serving as an alternative spectrum expression of the data to the traditional Fourier spectrum. The Hilbert Spectrum for the IMFs extracted from the sea surface salinity timeseries is shown in **Figure A3** with the original timeseries at the bottom. From this result we verify that indeed, the higher energy (amplitude) for the timeseries is found in the lower frequency modes, mainly the shelf-slope scale around 90min.

Once the signal variability scales have been obtained, the next step consists of determining the forces responsible for this oscillation and/or obtaining the correlation between different variables. The problem with this is to obtain a correlation that is compatible with the type of assumption we make in EEMD. That is, a method that assumes the possibility of (i) the existence of mixtures of scales in the same signal; (ii) that the behavior of a scale can depends on time and (iii) that there are relationships that can vary with time within the same scale. Traditional correlation methods usually do not support these assumptions; therefore, Time-Dependent Intrinsic Correlation (TDIC) (Chen et al., 2010; Huang and Schmitt, 2014) emerges as a complementary tool to investigate correlations over time between two scales.

TDIC is based on the IMFs resulting from EMD/EEMD and has the same assumptions of non-linearity and non-stationarity of the signal. TDIC correlate over time two IMFs of different variables, with similar frequencies, on various time scales (i.e., time windows). The correlation over time is given by **Eq. A16**:

$$R_i(t_k^n) = Corr\left(c_{1i}(t_w^n), c_{2i}(t_w^n)\right) \qquad \textbf{(Eq. A16)}$$

Preprint not peer reviewed

This preprint research paper has not been peer reviewed. Electronic copy available at: https://ssrn.com/abstract=4861987

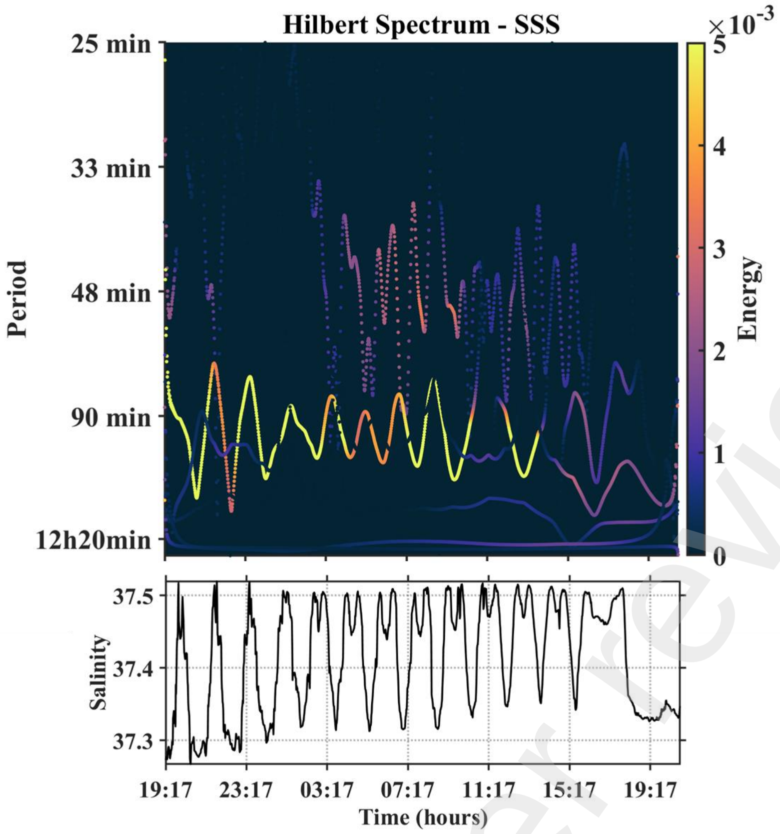

Figure A3. Hilbert Spectrum of the IMFs resulting from the Empirical Mode Decomposition of sea surface salinity timeseries. The colors represent the energy in terms of the square of the amplitude. The higher energy (higher amplitude) in this case is concentrated in low frequency modes (longer period); with periods oscillating around 90 min, corresponding to the shelf-slope scale.

Where c_{1i} and c_{2i} are the two IMFs investigated, t_w^n is the time window for the correlation, given by **Eq. A17** and n is any real positive number. The minimum window for calculating local correlation is given by **Eq. A18**, where T_{1i} e T_{2i} are the instantaneous periods of the two IMFs obtained through the zero-crossing method.

$$t_w^n = [t_k - nt_d/2 : t_k + nt_d/2] \qquad (\boldsymbol{Eq.\ A17})$$

$$t_d = \max\left(T_{1i}(t_k), T_{2i}(t_k)\right) \qquad (\boldsymbol{Eq.\ A18})$$

Student's t-test is also performed to investigate whether the difference between the correlation coefficient and zero is statistically significant. If the correlation does not pass the Student's t-test (p>0.5), a blank mask is placed in the correlation matrix. The result is a correlation matrix with statistical significance over time (x-axis) for each time window used to calculate the correlation index (y-axis) (Chen *et al*., 2010). **Figure A4** presents a simplified scheme of the joint EEMD/TDIC methodology.

See example of two time series decomposed by the EEMD (**Figure A4a**) and the resulting IMFs (**Figure A4b**). The resulting IMFs are evaluated in terms of the variance, i.e., how much of the original data variability (in percentage) is explained by each IMF (e.g., in **Figure A4c**, C5 explains 60.5% of the time series 1 and 18.5% of time-series 2). The result of the TDIC can be represented in two dimensions (e.g., **Figure A4d** right panel), where the x-axis is the time of the time-series, and the y-axis is the time-window used for the calculation of the correlation index, i.e., the timescales that range from the local period (local correlations at the bottom of the triangle in **Figure A4d**) to the whole time series (global correlation at the top of the triangle in **Figure A4d**). The correlation index calculated in the maximum

Preprint not peer reviewed

This preprint research paper has not been peer reviewed. Electronic copy available at: https://ssrn.com/abstract=4861987

time window is equivalent to the global correlation for the entire time series in traditional correlation methods.

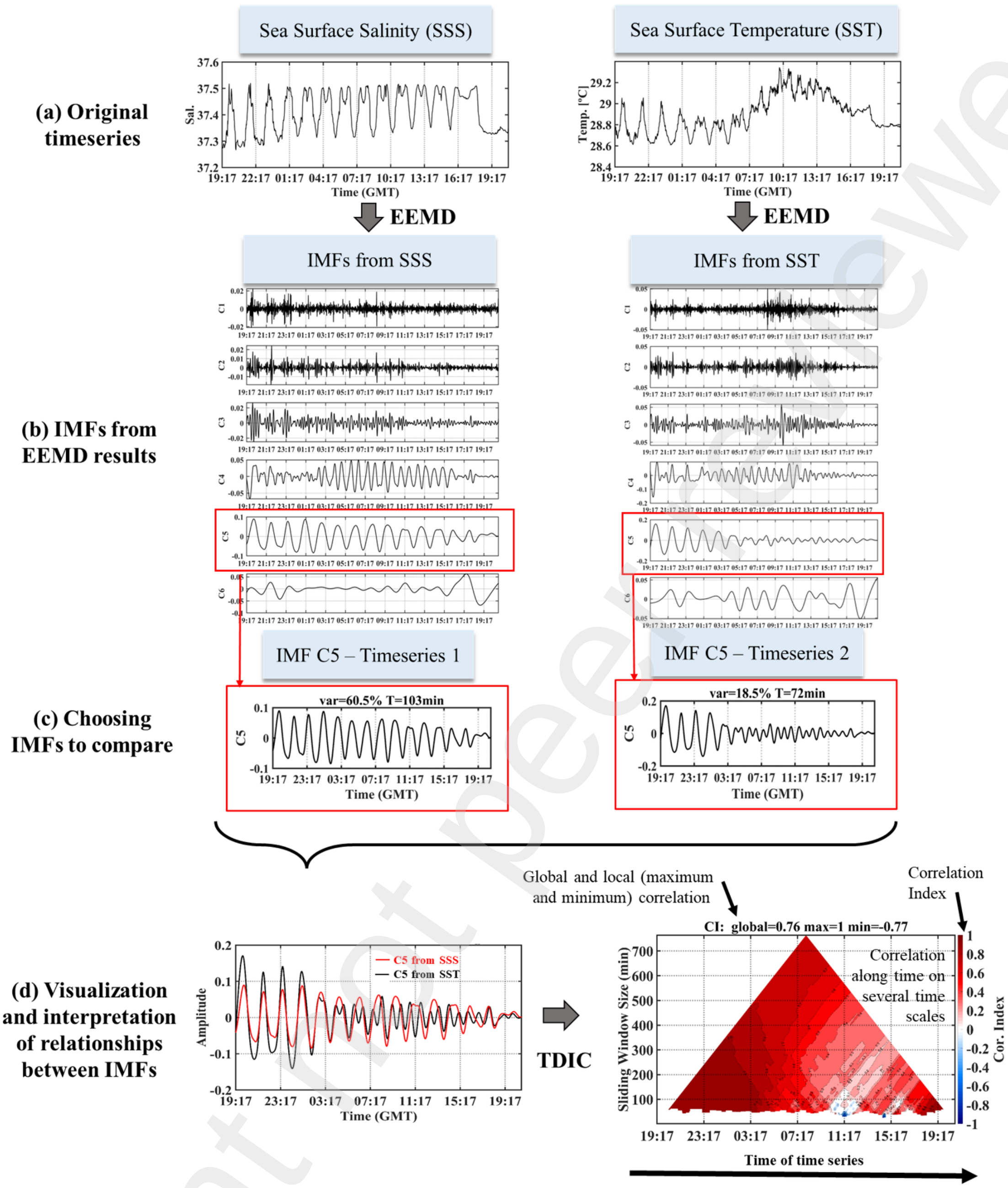

Figure A4. Example of the methodology applied to investigate the Multiple Rectangles Transect timeseries. (a) Two timeseries are decomposed through means of the EEMD method to obtain the respective (b) variability modes (i.e., the Intrinsic Mode Functions - IMFs). (c) The C5 mode of the Timeseries 1 was chosen to be compared with the C5 from timeseries 2 as they have close frequency modulation. The correlation of the signals in **(d)** are presented in the TDIC results (right panel). The colors represent the correlation index, that can be positive (correlation), null (no correlation) or negative (anticorrelation). The x-axis is the time of the timeseries, and the y-axis is the window size used for the correlation calculation, from the minimum local wave period (base of the triangle) to the maximum period corresponding to the whole timeseries (i.e., global correlation at the top of the triangle).

Comparing the modes (**Figure A4d**), we observe the higher amplitude of both at the beginning of the timeseries with the same phase and decrease of amplitude and change in frequency (mostly in timeseries 2) after 3:17 GMT, that if just after the sunrise. The signals become in phase again, still with small amplitude, at the end of the time series. For this example, we observe a strong local correlation that decreases along time and increase again at the end of the time series. This decrease in correlation in

Preprint not peer reviewed

This preprint research paper has not been peer reviewed. Electronic copy available at: https://ssrn.com/abstract=4861987

the middle of the time series, results in the global correlation 0.76, even though the local correlation at the beginning and the end of the time series reach the maximum value of 1, revealing the importance of the local correlation for this example.

We should point that, for correlations that are consistent (positive or negative) along the whole timeseries, the relationship could be represented by a simple correlation method. However, as observed from the results in section 3.2 (ii), the change in correlation of two IMFs along time can lead to low global correlations, which represent the correlation obtained from traditional methods, and sometimes to misleading interpretation, while TDIC can give a much more precise information about the changing relationship along time.

Acknowledgments

We acknowledge the French oceanographic fleet for funding the at-sea survey and the officers and crew of the R/V Antea for their contribution to the success of the operations during the ABRACOS cruises. S.Q. thank the support of the Conselho Nacional de Desenvolvimento Científico e Tecnológico (CNPq) through a PhD scholarship grant (140629/2020-3). M.A. thanks the Brazilian Research Network on Global Climate Change - Rede CLIMA (FINEP-CNPq 437167/2016-0) and the Brazilian National Institute of Science and Technology for Tropical Marine Environments - INCT AmbTropic (CNPq/FAPESB 565054/2010-4 and 8936/2011) for their support. This work is a contribution to the International Joint Laboratory TAPIOCA (www.tapioca.ird.fr) and to the TRIATLAS project, which has received funding from the European Union's Horizon 2020 research and innovation program under grant agreement No 817578.

References

Acha, E. M., Mianzan, H. W., Guerrero, R. A., Favero, M., & Bava, J. (2004). Marine fronts at the continental shelves of austral South America: Physical and ecological processes. *Journal of Marine Systems*, *44*(1–2), 83–105. https://doi.org/10.1016/j.jmarsys.2003.09.005

Aguiar, A. L., Cirano, M., Pereira, J., & Marta-Almeida, M. (2014). Upwelling processes along a western boundary current in the Abrolhos-Campos region of Brazil. *Continental Shelf Research*, *85*, 42–59. https://doi.org/10.1016/j.csr.2014.04.013

Aguiar, A. L., Cirano, M., Marta-Almeida, M., Lessa, G. C., & Valle-Levinson, A. (2018). Upwelling processes along the South Equatorial Current bifurcation region and the Salvador Canyon (13°S), Brazil. *Continental Shelf Research*, *171*, 77–96. https://doi.org/10.1016/j.csr.2018.10.001

Allen, J. S. (1980). Models of Wind-Driven Currents on the Continental Shelf. *Annual Review of Fluid Mechanics*, *12*(1), 389–433. https://doi.org/10.1146/annurev.fl.12.010180.002133

Araujo, M., Noriega, C., Medeiros, C., Lefèvre, N., Ibánhez, J. S. P., Flores Montes, M., Silva, A. C. da, & Santos, M. de L. (2019). On the variability in the CO2 system and water productivity in the western tropical Atlantic off North and Northeast Brazil. *Journal of Marine Systems*, *189*, 62–77. https://doi.org/10.1016/j.jmarsys.2018.09.008

Assunção, R. V., Silva, A. C., Roy, A., Bourlès, B., Henrique S. Silva, C., Ternon, J.-F., Araujo, M., & Bertrand, A. (2020). 3D characterisation of the thermohaline structure in the southwestern tropical

Preprint not peer reviewed

This preprint research paper has not been peer reviewed. Electronic copy available at: https://ssrn.com/abstract=4861987

Atlantic derived from functional data analysis of in situ profiles. *Progress in Oceanography*, 102399. https://doi.org/10.1016/j.pocean.2020.102399

Barth, J. A., Bogucki, D., Pierce, S. D., & Kosro, P. M. (1998). Secondary circulation associated with a shelfbreak front. *Geophysical Research Letters*, *25*(15), 2761–2764. https://doi.org/10.1029/98GL02104

Bertrand, A., Gerlotto, F., Bertrand, S., Gutiérrez, M., Alza, L., Chipollini, A., Díaz, E., Espinoza, P., Ledesma, J., Quesquén, R., Peraltilla, S., & Chavez, F. (2008a). Schooling behaviour and environmental forcing in relation to anchoveta distribution: An analysis across multiple spatial scales. *Progress in Oceanography*, *79*(2–4), 264–277. https://doi.org/10.1016/j.pocean.2008.10.018

Bertrand, S., Dewitte, B., Tam, J., Díaz, E., & Bertrand, A. (2008b). Impacts of Kelvin wave forcing in the Peru Humboldt Current system: Scenarios of spatial reorganizations from physics to fishers. *Progress in Oceanography*, *79*(2–4), 278–289. https://doi.org/10.1016/j.pocean.2008.10.017

Bertrand, A., Grados, D., Colas, F., Bertrand, S., Capet, X., Chaigneau, A., Vargas, G., Mousseigne, A., & Fablet, R. (2014). Broad impacts of fine-scale dynamics on seascape structure from zooplankton to seabirds. *Nature Communications*, *5*(1), 5239. https://doi.org/10.1038/ncomms6239

Bertrand, A. (2017). *ABRACOS 2 cruise*, *Antea R/V*. https://doi.org/10.17600/17004100

Brink, K. H. (2016). Cross-Shelf Exchange. *Annual Review of Marine Science*, *8*(1), 59–78. https://doi.org/10.1146/annurev-marine-010814-015717

Buarque, B. V., Barbosa, J. A., Magalhães, J. R. G., Cruz Oliveira, J. T., & Filho, O. J. C. (2016). Post-rift volcanic structures of the Pernambuco Plateau, northeastern Brazil. *Journal of South American Earth Sciences*, *70*, 251–267. https://doi.org/10.1016/j.jsames.2016.05.014

Cacchione, D. A. (2002). The Shaping of Continental Slopes by Internal Tides. *Science*, *296*(5568), 724–727. https://doi.org/10.1126/science.1069803

Camargo, J. M. R. de, Araújo, T. C. M. de,Maida, M., & Ushizima, T. M. (2007). Morfologia da plataforma continental interna adjacente ao município de Tamandaré, sul de Pernambuco - Brasil. *Revista Brasileira de Geofísica*, *25*, 79–89. https://doi.org/10.1590/S0102-261X2007000500008

Castelao, R. (2011). Intrusions of Gulf Stream waters onto the South Atlantic Bight shelf. *Journal of Geophysical Research: Oceans*, *116*(10), 1–10. https://doi.org/10.1029/2011JC007178

Chen, X., Wu, Z., & Huang, N. E. (2010). The Time-Dependent Intrinsic Correlation Based On the Empirical Mode Decomposition. *Advances in Adaptive Data Analysis*, *02*(02), 233–265. https://doi.org/10.1142/S1793536910000471

Cohen, L. (1995). Time-frequency analysis (Vol. 778). Prentice Hall PTR Englewood Cliffs.

Coutinho, P. N. (1996). Levantamento do estado da arte da pesquisa dos recursos vivos marinhos do Brasil: Oceanografia Geológica. Região Norte. *Relatório. Ministério do Meio Ambiente dos Recursos Hídricos e da Amazônia Legal. Programa REVIZEE. Brasília: MMA*.

Preprint not peer reviewed

This preprint research paper has not been peer reviewed. Electronic copy available at: https://ssrn.com/abstract=4861987

Davis, K. A., Leichter, J. J., Hench, J. L., & Monismith, S. G. (2008). Effects of western boundary current dynamics on the internal wave field of the Southeast Florida shelf. *Journal of Geophysical Research: Oceans, 113*(9), 1–15. https://doi.org/10.1029/2007JC004699

Denman, K. L., & Gargett, A. E. (1983). Time and space scales of vertical mixing and advection of phytoplankton in the upper ocean. *Limnology and Oceanography*, *28*(5), 801–815. https://doi.org/10.4319/lo.1983.28.5.0801

Dever, E. P. (1997). Wind-forced cross-shelf circulation on the Northern California shelf. *Journal of Physical Oceanography*, *27*(8), 1566–1580. https://doi.org/10.1175/1520-0485(1997)027<1566:WFCSCO>2.0.CO;2

Domingues, E. C., Schettini, C. A. F., Truccolo, E. C., & Oliveira Filho, J. C. (2017). Hydrography and currents on the Pernambuco Continental Shelf. *Revista Brasileira de Recursos Hidricos*, *22*(0). https://doi.org/10.1590/2318-0331.0217170027

Dossa, A. N., Silva, A. C., Chaigneau, A., Eldin, G., Araujo, M., & Bertrand, A. (2021). Near-surface western boundary circulation off Northeast Brazil. *Progress in Oceanography*, *190*, 102475. https://doi.org/10.1016/j.pocean.2020.102475

Eduardo, L. N., Frédou, T., Lira, A. S., Ferreira, B. P., Bertrand, A., Ménard, F., & Frédou, F. L. (2018). Identifying key habitat and spatial patterns of fish biodiversity in the tropical Brazilian continental shelf. *Continental Shelf Research*, *166*, 108–118. https://doi.org/10.1016/j.csr.2018.07.002

Egbert, G. D., & Erofeeva, S. Y. (2002). Efficient Inverse Modeling of Barotropic Ocean Tides. *Journal of Atmospheric and Oceanic Technology*, *19*(2), 183–204. https://doi.org/10.1175/1520-0426(2002)019<0183:EIMOBO>2.0.CO;2

Ekau, W., & Knoppers, B. (1999). An introduction to the pelagic system of the North-East and East Brazilian shelf. *Archive of Fishery and Marine Research*, *47*(2/3), 113–132.

Erofeeva, S. (2022). TPXO9v2 and TPXO9-atlas-v5: two new global barotropic tide models. *2022 Ocean Surface Topography Science Team Meeting*, 178.

Fournier, R. O., Marra, J., Bohrer, R., & Det, M. Van. (1977). Plankton Dynamics and Nutrient Enrichment of the Scotian Shelf. *Journal of the Fisheries Research Board of Canada*, *34*(7), 1004–1018. https://doi.org/10.1139/f77-153

Fox-Kemper, B., Adcroft, A., Böning, C. W., Chassignet, E. P., Curchitser, E., Danabasoglu, G., Eden, C., England, M. H., Gerdes, R., Greatbatch, R. J., Griffies, S. M., Hallberg, R. W., Hanert, E., Heimbach, P., Hewitt, H. T., Hill, C. N., Komuro, Y., Legg, S., Sommer, J. Le, … Yeager, S. G. (2019). Challenges and prospects in ocean circulation models. *Frontiers in Marine Science*, *6*(FEB), 1–29. https://doi.org/10.3389/fmars.2019.00065

Franzke, C. (2009). Multi-scale analysis of teleconnection indices: Climate noise and nonlinear trend analysis. *Nonlinear Processes in Geophysics*, *16*(1), 65–76. https://doi.org/10.5194/npg-16-65-2009

Preprint not peer reviewed

This preprint research paper has not been peer reviewed. Electronic copy available at: https://ssrn.com/abstract=4861987

Gawarkiewicz, G. (1991). Linear Stability Models of Shelfbreak Fronts. In *Journal of Physical Oceanography* (Vol. 21, Issue 4, pp. 471–488). https://doi.org/10.1175/1520-0485(1991)021<0471:lsmosf>2.0.co;2

Gawarkiewicz, G., Todd, R., Zhang, W., Partida, J., Gangopadhyay, A., Monim, M.-U.-H., Fratantoni, P., Malek Mercer, A., & Dent, M. (2018). The Changing Nature of Shelf-Break Exchange Revealed by the OOI Pioneer Array. *Oceanography*, *31*(1), 60–70. https://doi.org/10.5670/oceanog.2018.110

Genin, A. (2004). Bio-physical coupling in the formation of zooplankton and fish aggregations over abrupt topographies. *Journal of Marine Systems*, *50*(1–2), 3–20. https://doi.org/10.1016/j.jmarsys.2003.10.008

Grados, D., Bertrand, A., Colas, F., Echevin, V., Chaigneau, A., Gutiérrez, D., Vargas, G., & Fablet, R. (2016). Spatial and seasonal patterns of fine-scale to mesoscale upper ocean dynamics in an Eastern Boundary Current System. *Progress in Oceanography*, *142*, 105–116. https://doi.org/10.1016/j.pocean.2016.02.002

Gula, J., Molemaker, M. J., & McWilliams, J. C. (2015). Topographic vorticity generation, submesoscale instability and vortex street formation in the Gulf Stream. *Geophysical Research Letters*, *42*(10), 4054–4062. https://doi.org/10.1002/2015GL063731

Guo, L., van der Wegen, M., Roelvink, J. A., & He, Q. (2014). The role of river flow and tidal asymmetry on 1-D estuarine morphodynamics. *Journal of Geophysical Research: Earth Surface*, *119*(11), 2315–2334. https://doi.org/10.1002/2014JF003110

Haury, L. R., Yamazaki, H., & Itsweire, E. C. (1990). Effects of turbulent shear flow on zooplankton distribution. *Deep Sea Research Part A, Oceanographic Research Papers*, *37*(3), 447–461. https://doi.org/10.1016/0198-0149(90)90019-R

Herbert, G., Kermabon, C., Grelet, J., & Bourles, B. (2015). French PIRATA cruises S-ADCP data processing. *Mercator Ocean - Quaterly Newsletter*, *52*, 22–26. https://archimer.ifremer.fr/doc/00272/38320/

Holland, W. R. (1972). Baroclinic and topographic influences on the transport in western boundary currents. *Geophysical Fluid Dynamics*, *4*(1), 187–210. https://doi.org/10.1080/03091927208236095

Hu, D., Wu, L., Cai, W., Gupta, A. Sen, Ganachaud, A., Qiu, B., Gordon, A. L., Lin, X., Chen, Z., Hu, S., Wang, G., Wang, Q., Sprintall, J., Qu, T., Kashino, Y., Wang, F., & Kessler, W. S. (2015). Pacific western boundary currents and their roles in climate. *Nature*, *522*(7556), 299–308. https://doi.org/10.1038/nature14504

Huang, N. E., Shen, Z., Long, S. R., Wu, M. C., Snin, H. H., Zheng, Q., Yen, N. C., Tung, C. C., & Liu, H. H. (1998). The empirical mode decomposition and the Hilbert spectrum for nonlinear and non-stationary time series analysis. Proceedings of the Royal Society A: Mathematical, Physical and Engineering Sciences, 454(1971), 903–995. https://doi.org/10.1098/rspa.1998.0193

Preprint not peer reviewed

This preprint research paper has not been peer reviewed. Electronic copy available at: https://ssrn.com/abstract=4861987

Huang, N. E., Long, S. R., & Shen, Z. (1996). The Mechanism for Frequency Downshift in Nonlinear Wave Evolution. Advances in Applied Mechanics, 32(C). https://doi.org/10.1016/S0065-2156(08)70076-0

Huang, N. E., Shen, Z., & Long, S. R. (1999). A new view of nonlinear water waves: The Hilbert spectrum. Annual Review of Fluid Mechanics, 31, 417–457. https://doi.org/10.1146/annurev.fluid.31.1.417

Huang, N. E., Wu, Z., Long, S. R., Arnold, K. C., Chen, X., & Blank, K. (2009). On instantaneous frequency. Advances in Adaptive Data Analysis, 1(2), 177–229. https://doi.org/10.1142/S1793536909000096

Huang, Y., & Schmitt, F. G. (2014). Time dependent intrinsic correlation analysis of temperature and dissolved oxygen time series using empirical mode decomposition. *Journal of Marine Systems*, *130*, 90–100. https://doi.org/10.1016/j.jmarsys.2013.06.007

Huang, N. E., & Shen, S. S. P. (2014). Hilbert-Huang Transform and Its Applications (N. E. Huang & S. S. P. Shen (eds.); 2a, Vol. 5). World Scientific. http://www.worldscientific.com/doi/abs/10.1142/9789812703347_0001

Hummels, R., Brandt, P., Dengler, M., Fischer, J., Araujo, M., Veleda, D., & Durgadoo, J. V. (2015). Interannual to decadal changes in the western boundary circulation in the Atlantic at 11°S. *Geophysical Research Letters*, *42*(18), 7615–7622. https://doi.org/10.1002/2015GL065254

Huthnance, J. M. (1973). Tidal current asymmetries over the Norfolk Sandbanks. *Estuarine and Coastal Marine Science*, *1*(1), 89–99. https://doi.org/10.1016/0302-3524(73)90061-3

Huthnance, J. M. (1984). Slope Currents and "JEBAR." In *Journal of Physical Oceanography* (Vol. 14, Issue 4, pp. 795–810). https://doi.org/10.1175/1520-0485(1984)014<0795:sca>2.0.co;2

Huthnance, J. M. (1995). Circulation, exchange and water masses at the ocean margin: the role of physical processes at the shelf edge. *Progress in Oceanography*, *35*(4), 353–431. https://doi.org/10.1016/0079-6611(95)80003-C

IHO - International Hydrographic Organization. (2019). Standardization of Undersea Feature Names (Guidelines, Proposal Form Terminology). Edition 4.2.0 – October 2019. B-6, p. 45. International Hydrographic Organization. https://iho.int/uploads/user/pubs/bathy/B-6_e4 2 0_2019_EF_clean_3Oct2019.pdf

Jing, Z., & Wu, L. (2014). Intensified diapycnal mixing in the midlatitude western boundary currents. *Scientific Reports*, *4*, 1–6. https://doi.org/10.1038/srep07412

Joseph, A. (2014). Measuring Ocean Currents. In *Measuring Ocean Currents: Tools, Technologies, and Data*. Elsevier. https://doi.org/10.1016/C2011-0-05833-7

Kbaier Ben Ismail, D., Lazure, P., & Puillat, I. (2016). Application of Hilbert-Huang decomposition to temperature and currents data in the Réunion island. *OCEANS 2016 MTS/IEEE Monterey*, 1–9. https://doi.org/10.1109/OCEANS.2016.7761460

Preprint not peer reviewed

This preprint research paper has not been peer reviewed. Electronic copy available at: https://ssrn.com/abstract=4861987

Lamb, K. G. (2013). Internal Wave Breaking and Dissipation Mechanisms on the Continental Slope/Shelf. *Annual Review of Fluid Mechanics*, *46*(1), 231–254. https://doi.org/10.1146/annurev-fluid-011212-140701

Legg, S. (2014). Scattering of low-mode internal waves at finite isolated topography. *Journal of Physical Oceanography*, *44*(1), 359–383. https://doi.org/10.1175/JPO-D-12-0241.1

Lentz, S. J. (2001). The influence of stratification on the wind-driven cross-shelf circulation over the North Carolina shelf. *Journal of Physical Oceanography*, *31*(9), 2749–2760. https://doi.org/10.1175/1520-0485(2001)031<2749:TIOSOT>2.0.CO;2

Lentz, S. J., & Chapman, D. C. (2004). The importance of nonlinear cross-shelf momentum flux during wind-driven coastal upwelling. *Journal of Physical Oceanography*, *34*(11), 2444–2457. https://doi.org/10.1175/JPO2644.1

Lévy, M., Franks, P. J. S., & Smith, K. S. (2018). The role of submesoscale currents in structuring marine ecosystems. *Nature Communications*, *9*(1), 4758. https://doi.org/10.1038/s41467-018-07059-3

Li, Z., Wang, Y., Cheng, P., Zhang, G., & Li, J. (2016). Flood-ebb asymmetry in current velocity and suspended sediment transport in the Changjiang Estuary. *Acta Oceanologica Sinica*, *35*(10), 37–47. https://doi.org/10.1007/s13131-016-0923-9

Loder, J. W. (1980). Topographic Rectification of Tidal Currents on the Sides of Georges Bank. *Journal of Physical Oceanography*, *10*(9), 1399–1416. https://doi.org/10.1175/1520-0485(1980)010<1399:TROTCO>2.0.CO;2

Loder, J. W., & Wright, D. G. (1985). Tidal rectification and frontal circulation on the sides of Georges Bank. *Journal of Marine Research*, *43*(3), 581–604. https://doi.org/10.1357/002224085788440367

Macedo, S. J., Flores Montes, M. de J., Costa, K. M. P. (2009). Condições hidrológicas na zona econômica exclusiva do Nordeste do Brasil. In: *HAZIN, FHV. Meteorologia e Sensoriamento Remoto, Oceanografia Física, Oceanografia Química e Oceanografia Geológica*. *Programa REVIZEE – Score Nordeste*. Fortaleza, Ed. Martins & Cordeiro, vol. 1, 104-134.

Marra, J., Houghton, R. W., & Garside, C. (1990). Phytoplankton growth at the shelf-break front in the Middle Atlantic Bight. *Journal of Marine Research*, *48*(4), 851–868. https://doi.org/10.1357/002224090784988665

Martini, K. I., Alford, M. H., Kunze, E., Kelly, S. M., & Nash, J. D. (2011). Observations of internal tides on the oregon continental slope. *Journal of Physical Oceanography*, *41*(9), 1772–1794. https://doi.org/10.1175/2011JPO4581.1

Matano, R. P., & Palma, E. D. (2008). On the upwelling of downwelling currents. *Journal of Physical Oceanography*, *38*(11), 2482–2500. https://doi.org/10.1175/2008JPO3783.1

Mizobata, K., Saitoh, S. ichi, & Wang, J. (2008). Interannual variability of summer biochemical enhancement in relation to mesoscale eddies at the shelf break in the vicinity of the Pribilof Islands, Bering Sea. *Deep-Sea Research Part II: Topical Studies in Oceanography*, *55*(16–17), 1717–1728. https://doi.org/10.1016/j.dsr2.2008.03.002

Preprint not peer reviewed

This preprint research paper has not been peer reviewed. Electronic copy available at: https://ssrn.com/abstract=4861987

Munk, P., Larsson, P. O., Danielsen, D., & Moksness, E. (1995). Larval and small juvenile cod Gadus morhua concentrated in the highly productive areas of a shelf break front. *Marine Ecology Progress Series*, *125*(1–3), 21–30. https://doi.org/10.3354/meps125021

Nagai, T., Hasegawa, D., Tanaka, T., Nakamura, H., Tsutsumi, E., Inoue, R., & Yamashiro, T. (2017). First evidence of coherent bands of strong turbulent layers associated with high-wavenumber internal-wave shear in the upstream kuroshio. *Scientific Reports*, *7*(1), 1–14. https://doi.org/10.1038/s41598-017-15167-1

Nash, J. D., Alford, M. H., Kunze, E., Martini, K., & Kelly, S. (2007). Hotspots of deep ocean mixing on the Oregon continental slope. *Geophysical Research Letters*, *34*(1), 2–7. https://doi.org/10.1029/2006GL028170

Navrotsky, V. ., Lozovatsky, I. ., Pavlova, E. ., & Fernando, H. J. . (2004). Observations of internal waves and thermocline splitting near a shelf break of the Sea of Japan (East Sea). *Continental Shelf Research*, *24*(12), 1375–1395. https://doi.org/10.1016/j.csr.2004.03.008

Nazarian, R. H., & Legg, S. (2017). Internal wave scattering in continental slope canyons, Part 2: A comparison of ray tracing and numerical simulations. *Ocean Modelling*, *118*, 16–30. https://doi.org/10.1016/j.ocemod.2017.07.005

Nidzieko, N. J., & Ralston, D. K. (2012). Tidal asymmetry and velocity skew over tidal flats and shallow channels within a macrotidal river delta. *Journal of Geophysical Research: Oceans*, *117*(3), 1–17. https://doi.org/10.1029/2011JC007384

Oke, P. R., & Middleton, J. H. (2000). Topographically induced upwelling off Eastern Australia. *Journal of Physical Oceanography*, *30*(3), 512–531. https://doi.org/10.1175/1520-0485(2000)030<0512:TIUOEA>2.0.CO;2

Perrot, Y., Brehmer, P., Habasque, J., Roudaut, G., Behagle, N., Sarré, A., & Lebourges-Dhaussy, A. (2018). Matecho: An Open-Source Tool for Processing Fisheries Acoustics Data. *Acoustics Australia*, *46*(2), 241–248. https://doi.org/10.1007/s40857-018-0135-x

Pineda, J. (1994). Internal tidal bores in the nearshore: warm-water fronts, seaward gravity currents and the onshore transport of neustonic larvae. *Journal of Marine Research*, *52*(3), 427–458. https://doi.org/10.1357/0022240943077046

Prestes, Y. O., Silva, A. C. da, & Jeandel, C. (2018). Amazon water lenses and the influence of the North Brazil Current on the continental shelf. *Continental Shelf Research*, *160*(December 2016), 36–48. https://doi.org/10.1016/j.csr.2018.04.002

Robinson, I. S. (1981). Tidal vorticity and residual circulation. *Deep Sea Research Part A, Oceanographic Research Papers*, *28*(3), 195–212. https://doi.org/10.1016/0198-0149(81)90062-5

Rochford, D. J., 1991. 'Upwelling': does it need a stricter definition? Australian Journal of Marine and Freshwater Research 42, 45–46.

Preprint not peer reviewed

This preprint research paper has not been peer reviewed. Electronic copy available at: https://ssrn.com/abstract=4861987

Roughan, M., & Middleton, J. H. (2002). A comparison of observed upwelling mechanisms off the east coast of Australia. *Continental Shelf Research*, *22*(17), 2551–2572. https://doi.org/10.1016/S0278-4343(02)00101-2

Schaeffer, A., Roughan, M., & Morris, B. D. (2013). Cross-Shelf Dynamics in a Western Boundary Current Regime: Implications for Upwelling. *Journal of Physical Oceanography*, *43*(5), 1042–1059. https://doi.org/10.1175/jpo-d-12-0177.1

Schneider, D. (1982). Fronts and Seabird Aggregations in the Southeastern Bering Sea. *Marine Ecology Progress Series, 10*, 101–103. https://doi.org/10.3354/meps010101

Schott, F. A., Brandt, P., Hamann, M., Fischer, J., & Stramma, L. (2002). On the boundary flow off Brazil at 5-10°S and its connection to the interior tropical Atlantic. *Geophysical Research Letters*, *29*(17), 21-1-21–24. https://doi.org/10.1029/2002GL014786

Schott, F. A., Dengler, M., Zantopp, R., Stramma, L., Fischer, J., & Brandt, P. (2005). The shallow and deep western boundary circulation of the South Atlantic at 5°-11°S. *Journal of Physical Oceanography*, *35*(11), 2031–2053. https://doi.org/10.1175/JPO2813.1

Shears, N. T., & Bowen, M. M. (2017). Half a century of coastal temperature records reveal complex warming trends in western boundary currents. *Scientific Reports*, *7*(1), 1–9. https://doi.org/10.1038/s41598-017-14944-2

Silva, M., Araújo, M., Servain, J., & Pierrick, P. (2009a). Circulation and heat budget in a regional climatological simulation of the Southwestern Tropical Atlantic. *Tropical Oceanography*, *37*(1–2). https://doi.org/10.5914/tropocean.v37i1-2.5156

Silva, M., Araujo, M., Servain, J., Penven, P., & Lentini, C. A. D. (2009b). High-resolution regional ocean dynamics simulation in the southwestern tropical Atlantic. *Ocean Modelling*, *30*(4), 256–269. https://doi.org/10.1016/j.ocemod.2009.07.002

Silva, M., Ferreira, B., Maida, M., Queiroz, S., Silva, M., Varona, H. L., Araújo, T. C. M., & Araújo, M. (2021). Flow-topography interactions in the western tropical Atlantic boundary off Northeast Brazil. *Journal of Marine Systems*, 103690. https://doi.org/10.1016/j.jmarsys.2021.103690

Stern, M. E., & Shen, C. Y. (1975). Displacement and rectification of planetary fluids. In *Geophysical Fluid Dynamics* (Vol. 7, Issue 1). https://doi.org/10.1080/03091927508242614

Stramma, L., & England, M. (1999). On the water masses and mean circulation of the South Atlantic Ocean. *Journal of Geophysical Research: Oceans*, *104*(C9), 20863–20883. https://doi.org/10.1029/1999JC900139

Stramma, L., Fischer, J., & Reppin, J. (1995). The North Brazil Undercurrent. *Deep Sea Research Part I: Oceanographic Research Papers*, *42*(5), 773–795. https://doi.org/10.1016/0967-0637(95)00014-W

Todd, R. E., Chavez, F. P., Clayton, S., Cravatte, S. E., Goes, M. P., Graco, M. I., Lin, X., Sprintall, J., Zilberman, N. V., Archer, M., Arístegui, J., Balmaseda, M. A., Bane, J. M., Baringer, M. O., Barth, J. A., Beal, L. M., Brandt, P., Calil, P. H., Campos, E., … Zhang, L. (2019). Global perspectives on

Preprint not peer reviewed

This preprint research paper has not been peer reviewed. Electronic copy available at: https://ssrn.com/abstract=4861987

observing ocean boundary current systems. In *Frontiers in Marine Science* (Vol. 6, Issue JUL). Frontiers Media S.A. https://doi.org/10.3389/fmars.2019.00423

Urbano, D.F., De Almeida, R.A.F., Nobre, P., (2008). Equatorial Undercurrent and North Equatorial Countercurrent at 38°W: a new perspective from direct velocity data. *Journal of Geophysical Research.* 113, 4041. https://doi.org/10.1029/2007JC004215

Veleda, D., Araújo, M., Silva, M., & Montagne, R. (2011). Seasonal and interannual variability of the southern south Equatorial Current bifurcation and meridional transport along the eastern brazilian edge. *Tropical Oceanography*, *39*(1), 27–59. https://doi.org/10.5914/to.2011.0051

Weatherall, P., Marks, K. M., Jakobsson, M., Schmitt, T., Tani, S., Arndt, J. E., Rovere, M., Chayes, D., Ferrini, V., & Wigley, R. (2015). A new digital bathymetric model of the world's oceans. Earth and Space Science, 2(8), 331–345. https://doi.org/10.1002/2015EA000107

Wu, L., Cai, W., Zhang, L., Nakamura, H., Timmermann, A., Joyce, T., McPhaden, M. J., Alexander, M., Qiu, B., Visbeck, M., Chang, P., & Giese, B. (2012). Enhanced warming over the global subtropical western boundary currents. *Nature Climate Change*, *2*(3), 161–166. https://doi.org/10.1038/nclimate1353

Wu, Z., & Huang, N. E. (2009). Ensemble Empirical Mode Decomposition: A Noise-Assisted Data Analysis Method. *Advances in Adaptive Data Analysis*, *01*(01), 1–41. https://doi.org/10.1142/S1793536909000047

Yanagi, T. (1987). Classification of "siome", streaks and fronts. *Journal of the Oceanographical Society of Japan*, *43*(3), 149–158. https://doi.org/10.1007/BF02109215

Yoon, B., & Woo, S.-B. (2013). Tidal asymmetry and flood/ebb dominance around the Yeomha channel in the Han River Estuary, South Korea. *Journal of Coastal Research*, *165*, 1242–1246. https://doi.org/10.2112/SI65-210.1

Zembruscki, S. G., Barreto, H. T., Palma, J. C., Milliman, J. D. (1972). Estudo preliminar das províncias geomorfológicas da margem continental brasileira. In: *Anais do Congresso Brasileiro De Geologia*, v. 26, p. 187–209.

Preprint not peer reviewed

This preprint research paper has not been peer reviewed. Electronic copy available at: https://ssrn.com/abstract=4861987

Journal of Marine Systems

Supplementary Material for

Tidal contributions to shelf break dynamics in the South-western Tropical Atlantic

Syumara Queiroz[1,2], Marcus André Silva[1,2], Moacyr Araujo[1,2,3], Alex Costa da Silva[1,2] & Arnaud Bertrand[1,2,4]

[1]Laboratório de Oceanografia Física Estuarina e Costeira (LOFEC), Department of Oceanography, Universidade Federal de Pernambuco, Av. Arquitetura, 50740-550, Recife, Pernambuco, Brazil.

[2]IJL TAPIOCA: International Joint Laboratory - Tropical Atlantic Interdisciplinary laboratory on physical, biogeochemical, ecological and human dynamics. Federal University of Pernambuco, Av. Arquitetura, 50740-550, Recife, Pernambuco, Brazil.

[3]Brazilian Research Network on Global Climate Change – Rede CLIMA, 12227-010, São José dos Campos, São Paulo, Brazil.

[4]Institut de Recherche pour le Développement (IRD), MARBEC (Univ Montpellier, CNRS, Ifremer, IRD), 34203 Sète, France.

Corresponding author: Syumara Queiroz (syumaraqueiroz@hotmail.com)

Contents of this file

Captions for Video 1
Table S1
Figures S1 and S2

Preprint not peer reviewed

This preprint research paper has not been peer reviewed. Electronic copy available at: https://ssrn.com/abstract=4861987

Video 1. Time lapse of the location (red dot) and track (blue line) of the ship (top panel) during the multiple rectangles transect execution and simultaneous acquisition of bottom depth (middle panel) and current velocity (along- and cross-shelf on the bottom panel) data.

Preprint not peer reviewed

This preprint research paper has not been peer reviewed. Electronic copy available at: https://ssrn.com/abstract=4861987

Table S1. Complete table of IMFs obtained from Ensemble Empirical Mode Decomposition (EEMD) analysis. Values of variance (Var), averaged period (Period) and maximum amplitude (MA) are presented for IMFs of averaged cross-shelf (CSavg) and along-shelf (ASavg) velocities, cross-shelf (CS-TIDE) and along-shelf (CS-TIDE) current from tidal model TPXO 9 and Bottom depth (BOT). For the graphical results, see Supp. Figure S2, S3 and S4.

IMF	**Bottom depth (BOT)**		
	Var (%)	**Period**	**MA (m)**
C1	<1	5 min	45
C2	<1	8 min	45
C3	<1	17 min	62
C4	3.4	36 min	143
C5	93.3	1h43 min	457
C6	2.2	1h50 min	87
C7	<1	4h12 min	22
C8	<1	12h05 min	11

IMF	**CS-TIDE**			**AS-TIDE**		
	Var (%)	**Period**	**MA ($m.s^{-1}$)**	**Var (%)**	**Period**	**MA ($m.s^{-1}$)**
C1	<1	5min	<0.01	<1	5min	<0.01
C2	<1	10min	<0.01	<1	9min	<0.01
C3	1.5	32min	<0.01	1.2	30min	0.014
C4	12.5	55min	0.014	7.9	50min	0.041
C5	39.2	1h33min	0.020	20.4	1h26min	0.033
C6	1.8	2h06min	<0.01	1.7	2h9min	0.012
C7	44.6	12h27min	0.013	68.3	12h40min	0.038

IMF	**CS_{avg} velocity**			**AS_{avg} velocity**		
	Var (%)	**Period**	**MA ($m.s^{-1}$)**	**Var (%)**	**Period**	**MA ($m.s^{-1}$)**
C1	<1	5min	0.05	<1	6min	0.04
C2	2.9	9min	0.04	2.3	10min	0.06
C3	4.2	15min	0.05	3.3	19min	0.04
C4	10.2	43min	0.05	21.5	50min	0.09
C5	67.7	1h25min	0.12	26.6	1h37min	0.08
C6	4.8	2h33min	0.03	1.6	3h21min	0.02
C7	4.3	6h27min	0.03	44.4	12h39min	0.07
C8	5.1	12h24min	0.02	-	-	-

Preprint not peer reviewed

This preprint research paper has not been peer reviewed. Electronic copy available at: https://ssrn.com/abstract=4861987

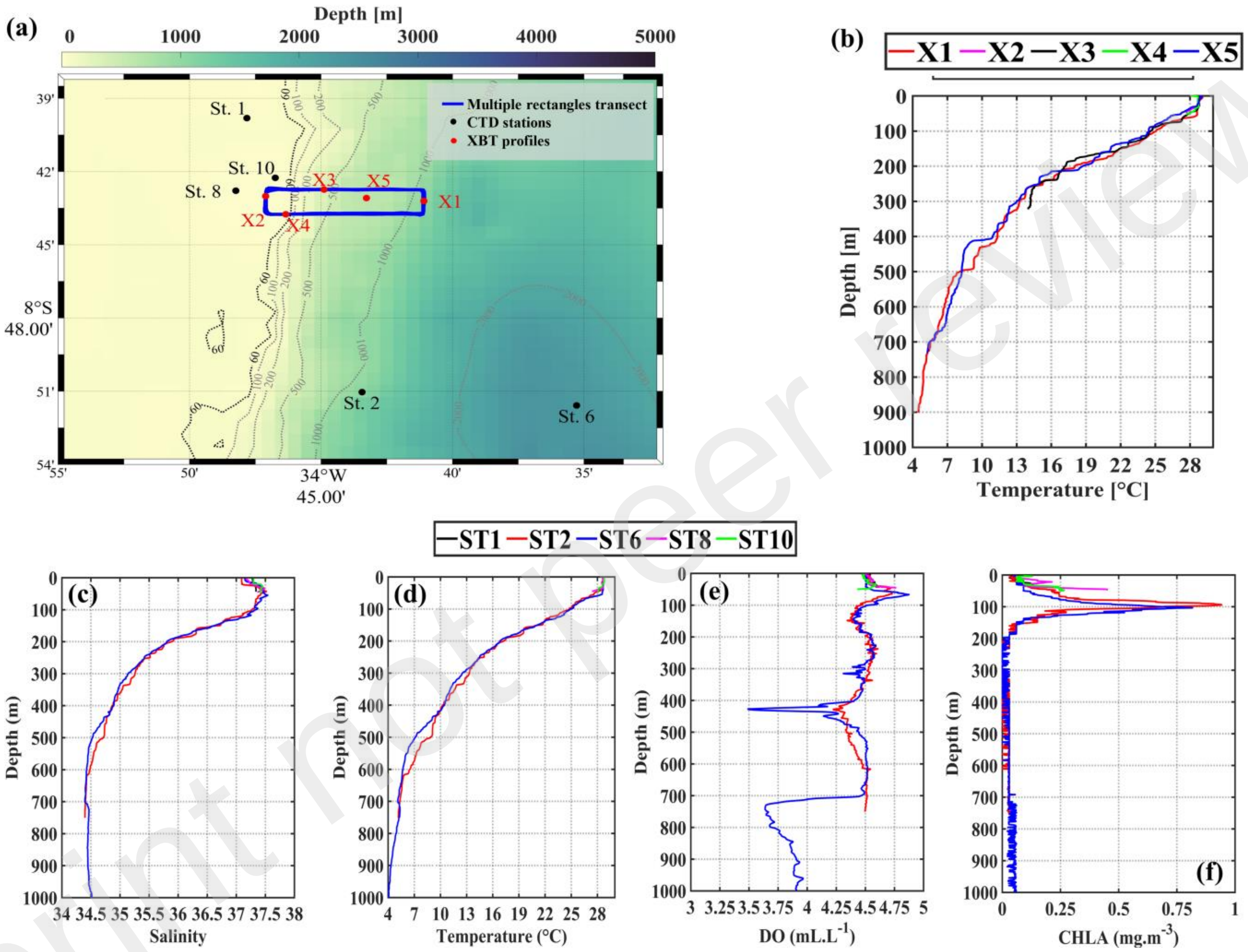

Figure S1. Location (a) of XBT (red dots) and CTD (black dots) stations in relation to the multiple rectangles transect (MRT). Vertical profiles of temperature (b) for XBTs X1 (red), X2 (magenta), X3 (black), X4 (green) and X5 (blue). Vertical profiles of salinity (c), temperature (d), dissolved oxygen (e) and chlorophyll-a concentration (f) for CTD stations ST1 (black), ST2 (red), ST6 (blue), ST8 (magenta) and ST10 (green); for XBTs X1 (red), X2 (magenta), X3 (black), X4 (green) and X5 (blue). CTDO stations were achieved on 09-04-2017 16:35, 09-04-2017 20:44, 11-04-2017 09:57, 11-04-2017 18:45 and 13-04-2017 01:16 GMT, respectively. XBTs were launched on 11-04-2017 23:16, 12-04-2017 00:09, 12-04-2017 00:27, 12-04-2017 01:41, 12-04-2017 21:10 GMT, respectively.

Preprint not peer reviewed

This preprint research paper has not been peer reviewed. Electronic copy available at: https://ssrn.com/abstract=4861987

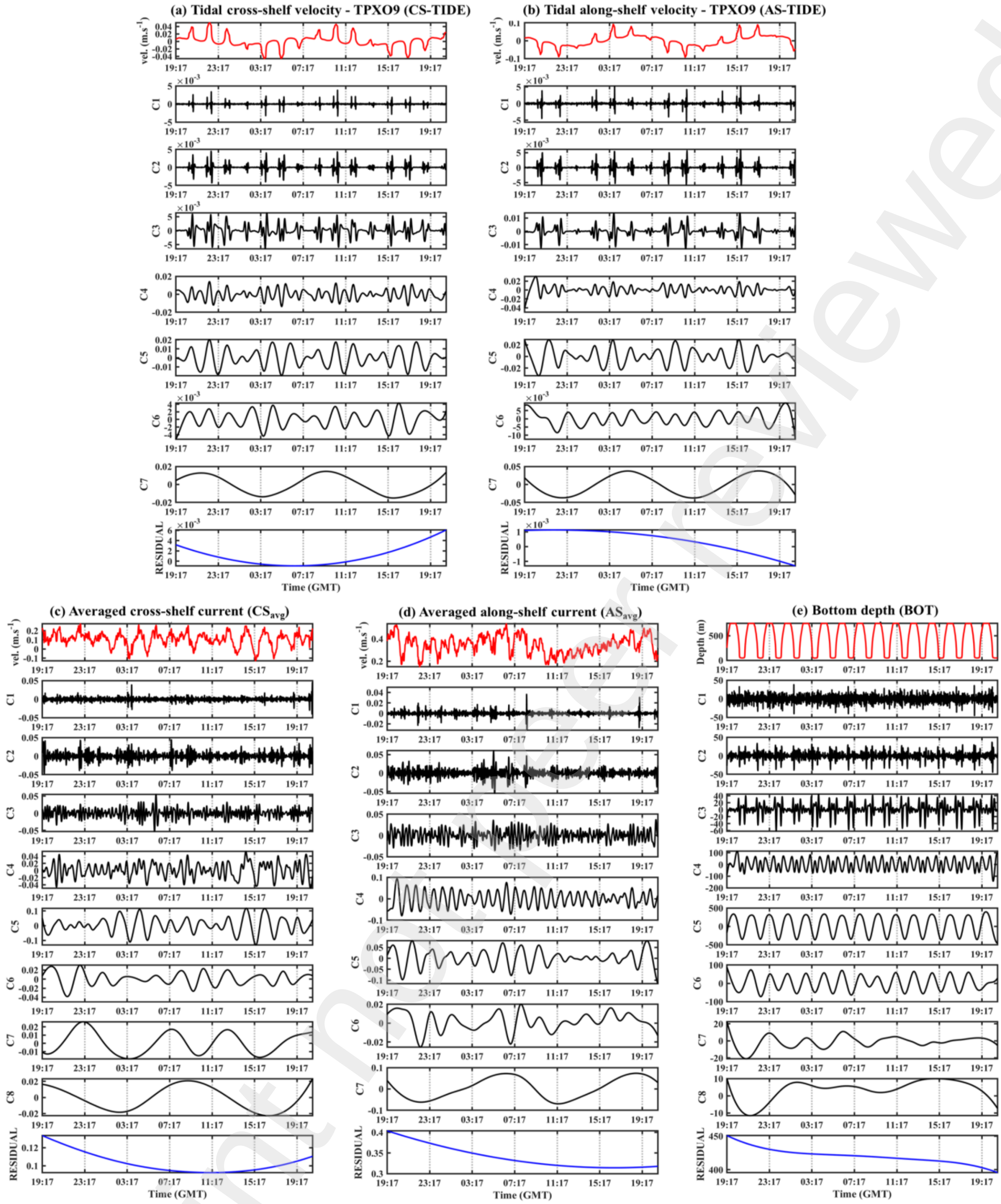

Figure S2. Ensemble Empirical Mode Decomposition results for the **(a)** cross-shelf tidal velocity (CS-TIDE) and **(b)** along-shelf tidal velocity (AS-TIDE) from the model TPXO9 for the same coordinates and time of the multiple rectangles transect (MRT); **(c)** cross-shelf velocity (CS_{avg}) and **(d)** along-shelf velocity (AS_{avg}) and; **(e)** bottom depth during the rectangle transect (MRT) experiment.C1 to C9 represent the components of the different variability scales. The residual of the composition represents the trend for the time-series.

This preprint research paper has not been peer reviewed. Electronic copy available at: https://ssrn.com/abstract=4861987